UiA University of Agder

Master

PERFORMANCE OF MOLYBDENUM DISULFIDE AS ANODE MATERIAL IN LITHIUM-ION BATTERIES

KRISTINE LEHRMANN SOLVANG

SUPERVISORS

Prof. Johannes Martin Landesfeind

Prof. Gunstein Skomedal

University of Agder, 2023

Faculty of Engineering and Science

Department of Engineering Sciences

Gruppeerklæring

1	Jeg erklærer herved at min besvarelse er mitt eget arbeid, og at jeg ikke har brukt andre kilder eller har mottatt annen hjelp enn det som er nevnt i besvarelsen	☑
2	Jeg erklærer videre at denne besvarelsen: - ikke har vært brukt til annen eksamen ved annen avdeling/universitet/ høgskole innenlands eller utenlands. - ikke refererer til andres arbeid uten at det er oppgitt. - ikke refererer til eget tidligere arbeid uten at det er oppgitt. - har alle referansene oppgitt i litteraturlisten. - ikke er en kopi, duplikat eller avskrift av andres arbeid eller besvarelse.	☑
3	Jeg er kjent med at brudd på ovennevnte er å betrakte som fusk og kan medføre annullering av eksamen og utestengelse fra universiteter og høgskoler i Norge, jf. §§4-7 og 4-8 og Forskrift om eksamen §§ 31.	☑
4	Jeg er kjent med at alle innleverte oppgaver kan bli plagiatkontrollert.	☑
5	Jeg er kjent med at Universitetet i Agder vil behandle alle saker hvor det foreligger mistanke om fusk etter høgskolens retningslinjer for behandling av saker om fusk.	☑
6	Jeg har satt meg inn i regler og retningslinjer i bruk av kilder og referanser på biblioteket sine nettsider	☑

Publiseringsavtale

Fullmakt til elektronisk publisering av oppgaven. Forfatterne har opphavsrett til oppgaven. Det betyr blant annet enerett til å gjøre verket tilgjengelig for allmennheten (Åndsverkloven. §2). Alle oppgaver som fyller kriteriene vil bli registrert og publisert i Brage Aura og på UiA sine nettsider med forfatternes godkjennelse. Oppgaver som er unntatt offentlighet er taushetsbelagt/konfidensiell vil ikke bli publisert.		
Jeg gir herved Universitetet i Agder en vederlagsfri rett til å gjøre oppgaven tilgjengelig for elektronisk publisering:	☑ Ja	☐ Nei
Er oppgaven båndlagt (konfidensiell)?	☐ Ja	☑ Nei
Er oppgaven unntatt offentlighet? (inneholder taushetsbelagt informasjon. Jfr. Offl. §13/Fvl. §13)	☐ Ja	☑ Nei

Acknowledgements

This thesis is the final part of the Renewable Energy masters program at the University of Agder at the Faculty of Engineering and Science. The work executed at the Department of Engineering Sciences as the last subject ENE-500 in the spring of 2023.

Since the beginning of my higher education, I have had an interest in batteries, and the establishment of Morrow Batteries in 2020 on the coast of south Norway did not make it less interesting. This semester I have been eagerly trying to wrap my head around battery research and in spite of many ups and downs, I come out on the other side still with more interest in the field. I hope this is not my last dealing with battery technology or research.

Throughout the work done in this thesis I have been in contact with many of the UiA staff and always got the help and support I needed. I am grateful for all the help I got, but I would like to give an extra special thanks to some of the key people that have helped me along the way.

I would like to thank my supervisors, prof. Johannes M. Landesfeind and prof. Gunstein Skomedal, for allowing and helping me to pursue this task. And especially Johannes for his good guidance, availability and willingness to explain things again and again, and for hiring a great team. A huge thanks to the ECBC team, Electrochemistry team at the Battery Coast, for taking me in and making me feel like a part of the team. Especially to Marlene, Mahla, Rafal and Ash for help in the lab, knowledge and making office hours and meetings ten times more fun. Thank you to senior engineer and lab supervisor Odin Kvam for guidance and insight when handling acid in the lab, and for patience when I tried to make a propper risk assessment.

I would also like to thank Andreas Sigervold for sending the molybdenum disulfide from Knaben Gruver. And as my last of five years at UiA come to an end, I would like to thank my great friend and supporter Ingrid Marie Skaug Lindqvist for help every step of the way.

Sammendrag

Målet med denne avhandlingen var å forberede og karakterisere det naturlige mineralet molybden disulfid fra den lokale gruven Knaben Gruver, for bruk som anodemateriale i litium-ion-batterier. Prosessen med å rense med svovelsyre, kulemølling og sikting produserte partiklene til størrelser under 45 mikrometer og ga få urenheter, materialet ble karakterisert ved testing som anode i en myntcelle. Det ble laget fire elektroder som ble satt sammen i myntceller med litium som motelektrode, to med et belegg av MoS_2 på 60 mikrometer tykkelse og to med et belegg på 30 mikrometer tykkelse. To celler, en av hver beleggtykkelse, ble testet mellom 0,2 VLi og 3 VLi, og to ble testet mellom 0,9 VLi og 3 VLi. Cellene som ble utladet til 0,2 VLi viste tegn til tap av aktivt materiale og økning i ionisk motstand på grunn av den reversible reaksjonen mellom MoS2 og litium som løser seg opp i Mo og Li2S under 0,6 VLi. Cellene viser en høyere kapasitet, over 700 mAh g−1, i den initielle litieringen ved C/10 enn den teoretiske kapasiteten, 669 mAh g^{-1}, på grunn av dannelse av SEI-laget. Kapasiteten reduseres imidlertid raskt ved sykling ved C/2. De tykkere elektrodene viser raskere nedbrytning, sannsynligvis på grunn av flere sidereaksjoner i cellen, og SEM-bildene viser mer sprekking av materialet i de tykkere cellene. Ved sykling av to celler mellom 0,9 VLi og 3 V_{Li} ble kapasiteten i cellen redusert, siden den eneste reaksjonen som gir kapasitet er litium innterkalering i MoS_2-lagene, denne reaksjonen gir bare 167 mAh g^{-1}, mens dannelse av SEI-laget gir litt mer kapasitet enn teoretisk. Den tynnere elektroden viste ingen tegn til tap av aktivt materiale eller økning i ionisk motstand etter første syklus, og mindre sprekking ble observert i SEM-bildene etter sykling. MoS_2 kan være et godt anodemateriale for litium batterier, men det kreves mer forskning for å forstå mekanismene ved litiering og delitiering. Ovenfra og ned tilnærmingen med kulemølling og testing av materialet gir en kapasitet som er nær den teoretiske ved lengre ladetider, men den raske nedbrytningen av cellen krever ytterligere forbedringer for å være egnet for kommersiell bruk.

Abstract

The goal of this thesis was to prepare and characterize the natural mineral molybdenum disulfide from the local mine Knaben Gruver, for use as anode material in lithium ion batteries. The process of purifying with sulfuric acid, ball milling and sieving the powder produced flaky particles of sizes below 45 µm with few impurities, which was characterized by coin cell testing. Four electrodes were assembled in coin cells with lithium as reference/counter electrode, two with 60 µm thickness coating and two with 30 µm thickness coating. Two cells, one of each coating thickness, were tested between 3 V_{Li} and 0.2 V_{Li} and two were tested between 3 V_{Li} and 0.9 V_{Li}. The cells discharged to 0.2 V_{Li} showed signs of active material loss and ionic resistance increase due to the reversible reaction of MoS_2 and lithium dissolving into Mo and Li_2S below 0.6 V_{Li}. The cells show a higher capacity, over 700 mAh g_{-1}, in the initial lithiation at C/10 than the theoretical capacity, 669 mAh g^{-1}, due to SEI layer forming, but the capacity decreases rapidly when cycled at C/2. The thicker electrodes show faster decay probably due to more side reactions happening in the cell and the SEM pictures show more cracking of the thicker cell. When cycling two cells between 3 V_{Li} and 0.9 V_{Li} the capacity of the cell was decreased due to the only reaction yielding capacity being lithium intercalation in the MoS_2 layers, this reaction only yields 167 mAh g^{-1}, whereas the SEI layer formation also gives a little more capacity than theoretical. The tinner electrode showed no sign of active material loss of ionic resistance increase after the first cycle and less cracking in the SEM pictures after cycling. The MoS_2 can be a good material for lithium ion anodes but need more research to understand the mechanisms when lithiated and delithiated. The top-down approach of ball milling and testing the material yields a capacity close to the theoretical one at longer charging times, but the fast decay of the cell needs more enhancement to be fit for commercial use.

Contents

List of Figures

List of Tables

1 Introduction

Energy storage technologies will be crucial to face both climate change [1] and the current energy crisis. Lithium-ion batteries (LIBs), as one technology for the reversible storage of electrical energy, have seen great advances in technology and a decline in price. This has made it possible to implement them widely in technologies such as electric vehicles [1] and stationary energy storage.

To meet the energy demand of electronic devices such as electrical vehicles, the electrode material needs to be able to fast charge [1], have more mechanical strength, and have higher energy density. The materials typically used are for now the ones that have shown the best combination of these as well as being available, cheap, and have long cycle life.

The main components in rechargeable batteries are their electrodes [2]. The electrodes are made with material with the ability to store energy in the form of lithium ions and electrons [3] and the compositions of these are very important. Much research has therefore gone into investigating electrode materials and enhancing the already used materials [2].

Today most anodes are made with graphite as their active material to hold lithium ions [4], in fact, 98% of all commercial lithium ion batteries use graphite anodes [5]. Research has been and is being done to enhance the performance of the graphite anode [2], but other materials are also on the brink of emerging as possible anode materials.

Researchers have been investigating the electrochemical properties of other layered structures such as MoS_2 since the 60s and 70s [6, 7]. In recent years, MoS_2 have been discussed and enhanced to fit lithium ion batteries [8]. This thesis will investigate the performance of molybdenum disulfide as active material in the negative electrode of lithium ion batteries.

The MoS_2 used in this thesis have been provided by the mine Knaben Gruver AS [9] in Kvinesdal, South Norway. The mine has been extracting molybdenum since 1885 [10] to use as a lubricant and had an important role in both world wars as provider for machinery. The mine was closed in 1973 but opened again on a small scale for a short period between 2005 and 2008 [10]. The MoS_2 extracted from Knaben is a natural mineral that holds a purity of 96-98% [9] with reported impurities of quartz, chalcopyrite and traces of other minerals like feldspar.

MoS_2 from the same provider has been prepared at the Univeristy of Agder previously as a bachelor thesis [11]. In 2021 MoS_2 powder was prepared and characterized with techniques such as SEM, EDS and XRD. The preparation methods did not yield particles of a size fit for battery anode testing and the electrochemical testing was therefore not done. The suggested future research on the MoS_2 from Knaben includes further removal of impurities [11], coin cell testing and electrochemical characterization, which will be the goal for this work.

For this thesis, the MoS_2 will be treated and prepared as a first step and electrochemically characterized as a second step. To prepare the MoS_2 for use in lithium-ion batteries the material in, powder form, will be ground by ball milling with ceramic balls and treated with sulfuric acid to wash out the impurities. The powder will then be mixed, coated and assembled into coin cells for electrochemically testing. To observe the mechanisms and performance of the electrodes the capacity found in testing will be compared to recent studies on MoS_2 anodes with different synthesis methods.

The approach used in this thesis is a top-down approach, meaning that MoS_2 is prepared from bigger particles [12]. This gives less control of the sizes and structures of the particles but can be a cheaper way of preparing the material than the opposite bottom-up method.

Problem definition

The main question of this thesis is; what are the electrochemical properties of top-down prepared and purified MoS_2 for use in lithium-ion batteries?

To answer this main question this thesis will try to focus on the three following research questions:

- What preparations and methods are needed to make anode material of MoS_2 from Knaben Gruver AS?
- What potential does MoS_2 have for use in lithium-ion batteries?
- What are the cyclability, stability, and disadvantages of using MoS_2 in lithium-ion batteries?

2 Theory

2.1 Battery components

The basic principle of a lithium-ion battery is the reversible motion of lithium ions between the electrodes during charge and discharge, while the electrons are forced to go through an external circuit and power the consumer the battery is connected to [13].

A commercial battery consists of electrodes, both a negative and a positive, an electrolyte, and a separator [14] [2]. Figure 1 shows an illustration of how a lithium-ion battery works [14].

The voltage of a cell is measured as the potential between the positive and the negative electrode [14]. The active material of the electrodes and the electrochemically active species (e.g. lithium ions) are therefore very important and chosen for their electrochemical properties. The positive electrode is called the cathode [15] and is made with metal oxides. The negative electrode is called the anode and is mostly constructed using graphite.

The material in which the electrodes are made is called the active material and is where the lithium-ions are stored in the battery [14]. The graphite in the anode is a layered material, and the lithium-ions are stored in between these layers. When the lithium-ions are stored in an electrode it is "lithiated" and when the lithium-ions are extracted the electrode is "delithiated".

The battery electrode stack in figure 1 has a current collector connected to the active material of the electrodes on the right and left[14]. The current collector is used as an electronic conductor, for the positive electrode it is typically made of aluminium and for the negative electrode made of copper. The active material is attached to the current collector to connect it to the battery terminals.

The two electrodes are separated by a electrically insulating separator [16], commercial LIBs use polyolefin separators for their low cost and mechanical properties. The separator allows for the lithium ions to travel through the cell between the electrodes. At the same time it forces the electrons to travel through the external circuit.

The electrolyte in the cell works as an ionic conductor and can be both liquid and solid, the most common is liquid [14]. The electrolyte does not conduct electrons and is electronically insolating. In the cell, the lithium ions can move back and forth between the electrodes. Because the electrolyte is not thermodynamically stable in the lithium-ion battery a passivation film forms during the first charges on the anode at voltages below 1.5 V_{Li}. This film is called the solid electrolyte interface or SEI layer. When the SEI layer forms some active lithium and electrolyte are consumed [17] resulting in some capacity loss and increased resistance in the battery cell. Much like the separator the SEI separates the two electrodes and when formed the supply of electrons at the SEI/electrolyte interface stops and with it the SEI formation, making it self limiting [18]. The layer helps to stabilize the battery.

When charged and discharged there are redox reactions happening in the cell [3] [19]. During charge, the ions are travelling from the cathode through the electrolyte and separator to the anode. During discharge, the lithium ions travel the opposite way, from the anode to the cathode. Oxidation is happening at the anode when discharged at the same time as there is a reduction at the cathode. When charged the reaction is the opposite as the anode is reduced and the cathode is oxidized.

One way to measure the potential of an electrochemically active material is to construct a half-cell

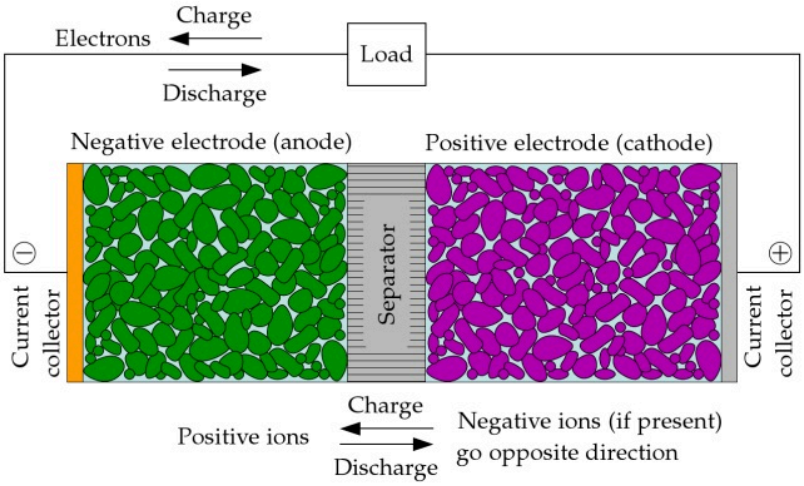

Figure 1: Schematic of a reversible battery electrode stack with main cell components: porous anode (green) supported on copper current collector (orange), porous separator avoiding electrical connection between the electrodes (grey), porous cathode (purple) supported on aluminium current collector (grey). During charge positive ions (and electrons through external circuit) move from cathode to anode (reprinted from Ref. [14])

.

[14]. A half cell contains one electrode with the material of interest [20], the working electrode, and one reference/counter electrode. In a half cell, the potential of the working electrode is measured against the potential of the reference/counter electrode, which is known. The reference/counter electrode can be metallic lithium, and for this thesis a metallic lithium foil is used as reference/counter electrode. Because of its high capacity lithium will not limit the capacity of the working electrode and will provide a stable reference potential.

2.2 Electrode materials

As previously mentioned the materials chosen for the negative and positive electrodes determine the battery performance. How many lithium atoms a material can store will determine the theoretical capacity of the electrode material. Graphite can, for instance, hold one lithium atom per six carbon atoms whereas silicon can hold 4 lithium per silicon atom. Using the number of lithium a material can store the theoretical capacity can be calculated. Equation 1 shows how the theoretical capacity is calculated using n as the number of lithium atoms stored, F is faradays constant (96 485 C mol^{-1}) and $M\mathrm{m}$ is the molar mass of the active material in g mol^{-1}.

$$\mathrm{Q} = \frac{n \cdot \mathrm{F}}{M\mathrm{m}} \tag{1}$$

For the positive electrode, the most commonly used materials are different lithium metal oxides [2], like LMO (lithium manganese oxide), LCO (lithium cobalt oxide), and NMC (lithium nickel cobalt manganese oxide), or phosphates like LFP (lithium iron phosphate).

As a negative electrode graphite has been the leading material since lithium-ion batteries were invented [5], holding 98% of the market share. The other 2% is held by LTO ($Li_4Ti_5O_{12}$) while other high-capacity anode materials, such as lithium metal, sulfides and oxides, are only being studied.

Graphite has great electronic conductivity [21], Myounggu Park et al. reported an electrical conductivity of polycrytalline graphite at 1000 S cm^{-1} [22], low cost [21], is available and has a layered structure for lithium intercalation. There are, however, drawbacks of the graphite anode. Graphite has the possibility to store one lithium ion per six carbon atoms, giving low theoretical capacity of 372 mAh g^{-1} [5]. During lithium intercalation of graphite, the interlayer spacing increases by 10%, posing a risk for mechanical stress on the battery cell. Other studied anode materials have higher capacities, such as silicon with 3578 mAh g^{-1}. Silicon, however, expands over 250% during charge/discharge [23], posing a great obstacle in lithium-ion batteries. Another drawback of the graphite anode is the inability to fast charge [24] and the material decaying with extensive cycling.

2.3 Molybdenum disulfide

The MoS_2 layers are connected by weak Van der Waals forces which makes it an excellent dry lubricant, just like graphite [25]. The hexagonally structured MoS_2 is used as a surface coating in machine parts, engines, and guns and as a lubricant in high-temperature conditions. The compound has a high-temperature tolerance and can be used at temperatures up to 350 °C in atmospheric conditions and 1100 °C in vacuum or inert conditions. A MoS_2 monolayer has two layers of sulfur atoms arranged in a hexagonal shape with one layer of molybdenum atoms in between. The molybdenum atoms can be arranged in a trigonal prismatic or octahedral shape.

Phases of molybdenum disulfide

MoS_2 has three main structural phases with different properties and structures. The metallic phase (1T) is an unstable phase, and its Mo-atoms are coordinated octahedrally and the suspension takes a dark grey colour. The 2H phase is a semiconducting phase, the structure of the Mo-atoms is trigonal prismatic in 2H, and as a suspension, the liquid takes a yellow or green shade. The 3R phase also has a trigonal prismatic arranged molybdenum-atom layer.

Figure 2 shows possible interlayer absorption sites for lithium ions in layers of MoS_2. Part (a) is the intercalation in the semiconducting 2H phase and part (b) is in the matallic 1T phase.

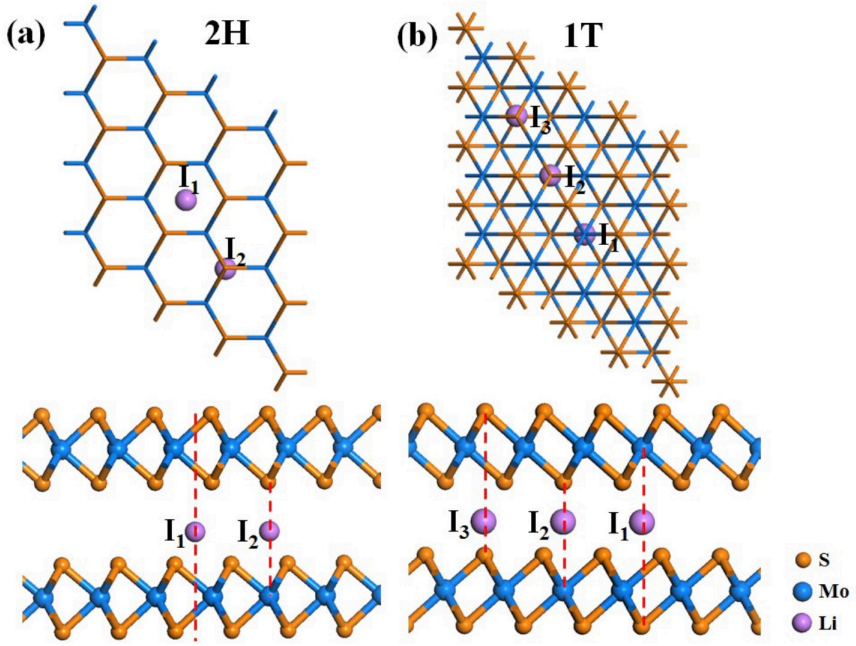

Figure 2: Top and side view of the structure of a single layer of molybdenum disulfide (reprinted from [26]) with lithium ion interlayer absorption sites as $I_{1,2,3}$ in phases 2H (a) and 1T (b) where the blue is molybdenum atoms, the yellow is sulfur atoms and purple is lithium.

2.3.1 Preparation methods

The main part of this thesis is the investigation of MoS2 from mineral sources for use in battery applications in a top-down approach. In the research literature the contrary approach, bottom-up is typically pursued. Different methods of both approaches are briefly summarized in the following paragraphs.

According to Junxiong et al., the four main methods of preparing MoS_2 in the nanoscale are exfoliation, chemical vapour deposition (CVD), hydro- and solvothermal synthesis, and thermal pyrolysis [12]. All of these approaches aim at making nanostructures of MoS_2 for use in batteries. As claimed by the authors the most promising one could be considered hydrothermal and thermal pyrolysis, in regards to delivering cheap material on a large scale, without stating specific details.

Of the four methods mentioned above, CVD and hydro-/solvothermal synthesis are considered bottom-up methods of synthesizing MoS_2 for batteries [12]. Bottom-up methods are synthesis methods in which the desired material is constructed from smaller particles or gas molecules [27]. The bottom-up method is a way of having control of the sizes and properties of the material that is being synthesized.

CVD for MoS_2 is a way of producing a controlled number of layers on a flat surface [12]. The process involves depositing films of materials on a substrate using vapour phases of precursor materials at a high temperature. Mo and S precursors, such as Mo or MoO_3 and vaporized S or H_2S gas, are used to make MoS_2 [12]. For example, researchers have used CVD to make a MoS_2-coated 3D graphene network and carbon-coated nano thorns of MoS_2 grown on carbon nanotubes [12].

Hydro- and solvothermal synthesis is a cheaper way of constructing multilayered nanosheets and nanocomposites [12]. The synthesis involves putting solutions with Mo and S precursors in a closed vessel and heating the solution under pressure. By this method, there have already been constructed structures such as nanoflowers, tubes, and spheres, as well as micro boxes [12]. The method has also proved useful to make MoS_2 hybrids, mostly with carbon.

Exfoliation and thermal pyrolysis is considered a top-down approach to the synthesis of MoS_2 for lithium-ion batteries. A top-down approach is where the material goes through a size reduction to fit its purpose [27]. It is a physical procedure where nanostructures are formed from bulk material.

With exfoliation MoS_2 nanosheets can be produced by mechanical cleavage, however, this method is limited by its low yield [12]. To increase the yield, chemical exfoliation has been developed. Bulk MoS_2 can be sonicated in N-methyl-pyrrolidone and dimethylformamide (DMF) to produce MoS_2 monolayers [12]. Another approach involves using alkali ions like Li^+, Na^+, and K^+ to intercalate between the layers of MoS_2, forming ion-intercalated MoS_2-based compounds. These compounds can be sonicated in water to obtain stable dispersion of 1T-MoS_2 nanosheets (see crystal structures of MoS2 in chapter 2.3, figure 2). Although this method produces nanosheets with high conductivity, the alkali ions introduced during the intercalation process are difficult to remove.

Thermal pyrolysis is another top-down approach to produce MoS_2 carbon composites, with techniques like electrospinning or spraying [12]. First, the MoS_2 material is mixed in with a polymer and heated up until it breaks down. The resulting MoS_2 nanosheets are trapped inside a carbon material, which makes a composite with a special structure. For example, ultrasmall MoS_2 plates were made by electrospinning and heating up a mixture of (NH_4) 2 MoS_4 and a polymer called PVP. PVP works as a dispersant for lithium-ion battery electrodes [28] and helps with the processing of conductive materials. Another example is MoS_2/graphene microspheres that were made by spray pyrolysis [12]. During the heating process, the (NH_4) 2 MoS_4 broke down and became MoS_2 nanosheets, while the polymers broke down into carbon and graphene, creating 3D microspheres. Table 1 shows the advantages and disadvantages of the four methods of synthesis of MoS_2 nanostructures mentioned above.

Table 1: Advatages and disadvantages of exfoliation, CVD, hydro-/solvethermal synthesis and thermal pyrolysis for preparing MoS_2, collected from a study in 2020 by Junxiong et al. [12].

Method	Structure	Advantages	Disadvantages
Exfoliation	Nanosheets	Cheap, simple, moderate to high quality, thin layers	Uncertain layer numbers, utilization of organic solvents, large size distribution
CVD	Nanosheets	Controllable, tunable layer numbers, high quality	Complex parameter control, low productivity, high temperature, high vacuum
Hyrdo-/ solvothermal	Nano sheets, flowers, rods, spheres	Uniform and controlled shapes, short processing time, low cost, high yield	High pressure, moderate crystallinity, organic solvents required
Thermal pyrolysis	Nanofibres from electrospinning, microspheres from spraying	Unifrom and controlled shapes, high crystallinity, good scalability	Moderate temperatures

2.3.2 Molybdenum disulfide in lithium-ion batteries

When MoS2 is used as an active material for lithium-ion batteries the lithium ions will be arranged between the layers of MoS_2 [12] as seen in figure 2. The interlayer distance of graphite (the most common anode material in LiBs) is approximately 0.34 nm, and the distance of MoS_2 layers is in comparison almost double at 0.62 nm [29]. The increased distance in the layers of MoS_2 compared to graphite gives the material no expansion at a fast solid diffusion of lithium in the material [8].

There are two reactions happening when charging a lithium-ion battery with a MoS_2 anode [30]. The first reaction reportedly occurs when the battery is charged between 3 V_{Li} and 1.1 V_{Li} [30] for the initial cycle where the lithium ions are intercalated between the layers of the MoS_2. This reaction also corresponds to the first plateau seen in the voltage capacity profiles of MoS_2 anodes (see, e.g., figure 3 red line up to 175 mAh/g). Equation 2 is the reaction equation of the lithiation of the MoS_2.

$$MoS_2 + Li^+ + e^- \rightarrow LiMoS_2 \tag{2}$$

Equation 1 with reaction equation 2 gives the following theoretical capacity:

$$Q = \frac{1 \cdot 96485.33C\ mol^{-1}}{3600s\ h^{-1} \cdot 160.07g\ mol^{-1}} \cdot 1000mA\ A^{-1} = 167.44mAh\ g^{-1}$$

The second reaction reported to occur with a MoS_2 anode is the LiMoS2 material dissolving into lithium-sulfur and molybdenum [30]. This happens at 0.6 V_{Li} and is seen as the second plateau in

the initial lithiation of the MoS_2 (see figure 3, red line from 175 mAh/g to 600 mAh/g). Equation 3 is the reaction equation of the second step of the intercalation, each molecule of MoS_2 can contain four lithium atoms in total.

$$LiMoS_2 + 3Li^+ + 3e^- \rightarrow 2Li_2S + Mo \tag{3}$$

The second plateau is associated with $LiMoS_2$ dissolving into lithium sulfur and molybdenum as shown in equation 3. The theoretical capacity of the full conversion reaction can also be calculated using equation 1, based on the storage of three more lithium atoms:

$$Q = \frac{3 \cdot 96485.33C\ mol^{-1}}{3600s\ h^{-1} \cdot 160.07g\ mol^{-}1} \cdot 1000mA\ A^{-1} = 669.74mAh\ g^{-1}$$

Due to this high theoretical capacity researchers have investigated the suitability of MoS2 for the use in LIBs. Some of the main findings will be presented in the next paragraphs.

As a substitute for graphite, extensive research has been done on silicon and tin because of their high theoretical specific capacity at 4200 mAh g^{-1} and 994 mAh g^{-1} respectively [31]. The drawbacks of these metals are great volume expansion when charged and discharged many times. MoS_2 resembles graphite but has a greater theoretical capacity and no expansion when cycling. The studies of molybdenum disulfide nanopowder by Farabi Bozheyev et al. [31] states that the material shows great potential for battery use based on the electrochemical characterisation explained in the next paragraph.

In the study by Farabi Bozheyev et al., molybdenum nanopowder was created by exploding molybdenum wires in argon gas [31]. The powder was then mixed with sulfur powder and pressed into a pellet. This pellet was placed in a reactor under high pressure and ignited. After the reaction, the resulting pellet was ground into smaller particles to obtain molybdenum disulfide nanopowder. The electrochemical performance on the MoS_2 nanopowder was measured by building a coin cell with lithium metal as a reference/counter electrode and cycled between 0.01 V_{Li} and 3 V_{Li}. Figure 3 shows the results of the three first cycles of this study of MoS_2. The first lithiation cycle shows two plateaus, one at 1 V_{Li} and one at 0.6 V_{Li}. The first plateau is the reaction in which the lithium intercalates in the MoS_2 to form Li_xMoS_2 and the second is where material decomposes to Mo and Li_2S. For the next 2 lithiations, there are three plateaus appearing at 2 V_{Li}, 1.3 V_{Li}, and 0.5 V_{Li} due to multi-step insertion of lithium. The delithiation process has one plateau reaching from 2.2 V_{Li} to 2.4 V_{Li}. The reported irreversible loss of capacity is 17.7% and is due to the solid electrolyte interface forming. The coulombic efficiency increases from 82.3% in the first cycle to 93.3% in the third cycle.

In 2022 MoS_2 was investigated as anode material in lithium-ion batteries by Xuan Wei et al. [32]. In this study, MoS_2 is constructed as foam. MoS_2 powder in bulk form is chemically exfoliated into nanosheets, which are dispersed into a mixture of alcohol and water. With copper as the current collector, the nanosheets are printed onto a heated collector as a thin film. Through solvent evaporation, the nanosheets self-assemble into a 3D porous structure with various morphologies. The resulting 3D architected MoS_2 foam exhibits hierarchical porous features and structural elements. This manufacturing process provides control over the formation of the porous network of the foam

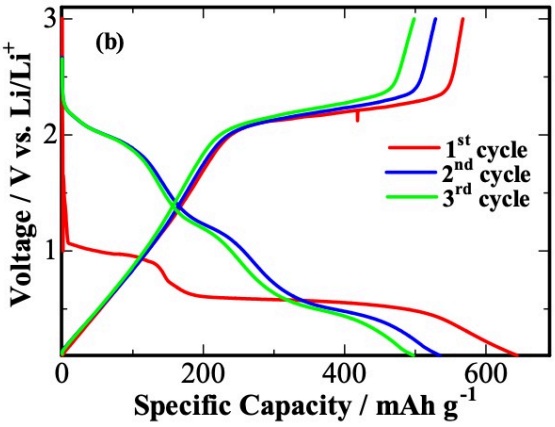

Figure 3: Voltage capacity profile of cycle 1, 2, and 3 of a cell constructed with MoS_2 nanopowder in 2017 tested by Farabi Bozheyev et al. in a coin cell of 1.12 mAh cm^2 loading, at room temperature, and at a C-rate of C/14. The MoS_2 was cycled in the voltage window 0.01 V_{Li} to 3 V_{Li} [31].

in a bottom-up type of synthesis. The study finds that this method of synthesizing an electrode makes the MoS_2 stick to the current collector in a firm way, this indicates the formation of uninterrupted conductive pathways. Figure 4 shows the specific capacity of foam MoS_2 plotted against the potential vs. lithium. The graph shows a very high specific capacity at over 1500 mAh g^{-1} for the first 10 cycles. The high capacity of the cell is explained as an additional last step in the discharge of the MoS_2 electrode where the lithium reacts with the sulfur to Li_2S giving the theoretical capacity of sulfur at 1675 mAh g^{-1}. The tests are done with different currents for 100 cycles resulting in the lowest specific capacity at 1111 mAh g^{-1} for higher currents and bouncing back to around 1500 mAh g^{-1} with lower currents.

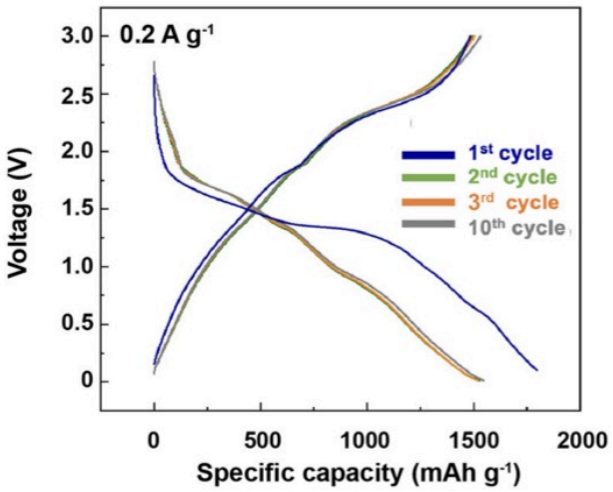

Figure 4: Voltage capacity profile of an electrode made with MoS_2 foam by Xuan Wei et al. in 2022, the cell was cycled at different C-rates, the one illustrated being C/8 and the graph is showing cycle 1, 2, 3, and 10 [32].

Another study on molybdenum disulfide shows the performance of silicon-protected nanosheets in lithium-ion batteries, the study by Jun-Seob Park et al. [33] was conducted in 2023. Molybdenum

disulfide was prepared as a thin film through a variant of chemical vapour deposition(CVD) called metal-organic CVD, and coated with silicon through radio frequency sputtering. The reason for coating the MoS_2 with silicon is the lithium loss happening when the reaction of MoS_2 + Li_x becomes Li_2S + Mo during lithiation. The MoS_2 is vertically grown on a stainless steel substrate and used as an electrode. The silicon layer was 30 nm thick on top of the MoS_2. A half-cell was assembled with the MoS_2 electrode and lithium metal as a reference/counter electrode, and the cell tested between 0.01 V_{Li} and 3 V_{Li}. Figure 5 show the results from cycling one cell with coating and one cell without at C/10. The initial specific capacity of the coated cell was 1997 mAh g^{-1} and the un-coated one was 1412 mAh g^{-1}. By evaluating the initial coulombic efficiencies of the coated MoS_2 and the un-coated MoS_2 it was found that the silicon coating had more than one positive effect. The layer prevented the dissolution of the MoS_2 [33] to Li_2S and increased the specific capacity of the cell. The two tested electrodes show peaks when lithiated, at 0.54 V_{Li}, 1.13 V_{Li}, and at 1.29 V_{Li}, associated with the insertion of lithium ions and with the reaction of MoS_2 dissolving into Mo and Li_2S. The main takeaway from this study is that by coating the MoS_2 with silicon the electrode was able to obtain a higher capacity and react better to extensive cycling. It is stated that the method could be applied to advanced thin-film batteries.

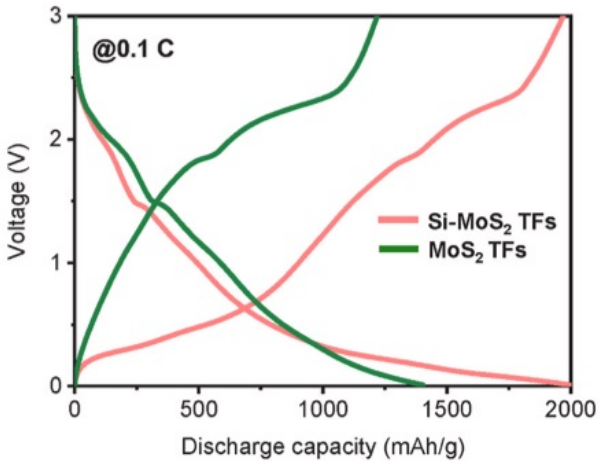

Figure 5: Voltage capacity profile of one electrode with silicon coated MoS_2 nanosheets, pink curve, and one MoS_2 electrode without coating, green curve, cycled at C/10 conducted by Jun-Seob Park et al. [33].

The three studies mentioned above show how molybdenum disulfide potentially can give a high capacity as an electrode in lithium-ion batteries. The specific capacity of both foam MoS_2 and thin-film MoS_2 provide a much higher value than that of graphite.

2.3.3 Prestudy at UiA

In 2021 Knaben Gruver AS in Kvinesdal, Norway sent samples of molybdenum disulfide mineral/ore to the University of Agder (UiA) [11] for preparation and investigation for use in lithium-ion batteries as part of a BSc thesis project. The sample was prepared but not tested as anode material due to limited time. This thesis is therefore an extension of the work previously done at UiA. The sample prepared in 2021 was ball milled for 24 hours with ceramic balls with diameters of 20 mm, 10 mm, and 5 mm. The particles from this ball milling process ranged mostly between 30 µm and 250 µm as can be seen in figure 6 [11]. The sizes of these particles are not fit to be used in lithium-ion batteries where typical particle sizes are around 5-20 µm and more milling is suggested for the powder to fit this purpose.

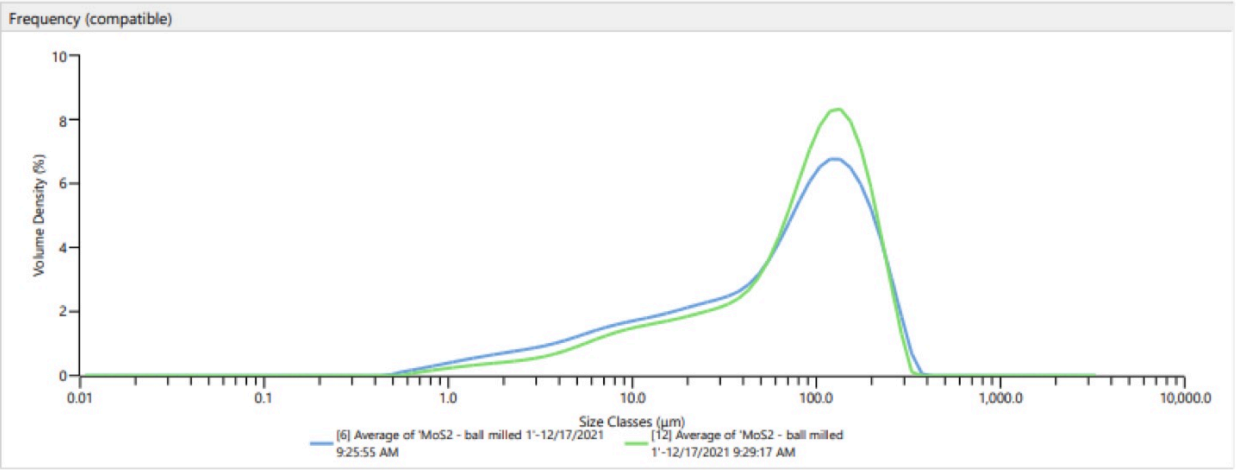

Figure 6: PSD analysis, measured by Malvern MASTERSIZER 3000, of MoS_2 powder prepared in 2021 [11] dissolved in water with ultrasonication, the majority of particles being in the size range of 30 µm to 250 µm.

It was found that the impurities in the molybdenum disulfide powder were SiO_2 and $CuFeS_2$ [11], silicon oxide (silica), and copper iron sulfide(chalcopyrite). The MoS_2 sample from 2021 was treated with sulfuric acid to remove iron and copper impurities. The treatment did, however, not remove all the metal impurities in the powder, it was therefore suggested to use another method of removing the iron called oxalic acid leaching.

Figure 7 shows an EDS mapping of the elements in the MoS_2 powder from 2021 [11]. The high percentage of carbon is the carbon tape that the sample is mounted on top of. Oxygen and silicon form silica, which is used in batteries and is therefore not considered an issue in battery testing. The analysis shows that the contamination of copper and iron is present in the material, which could be a problem. Aluminium and sodium traces in the mapping is explained as an effect of unclean scanning instruments.

XRD was performed on six samples, two ball-milled purified samples(1-2) [11], one normal sample(N), one milled sample(M), and two non-milled purified samples(3-4). The analysis shows that the ball-milled and non-ball-milled samples are more or less homogeneous due to little variations in diffraction peaks. The difference in the peak intensities in the milled and non-milled samples is explained by the acid treatment having more effect on the milled powder. The purified samples all show strong diffraction peaks indicating that they are highly crystalline. The XRD is compared to

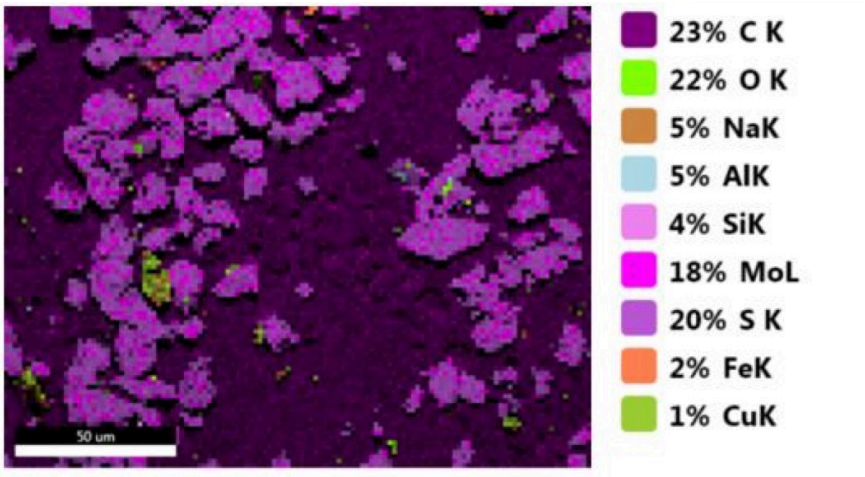

Figure 7: EDS mapping of MoS_2 powder from 2021 [11], the main impurities are Na, Al, Fe, and Cu.

three example samples and shows similarities to the hexagonal phase of molybdenum disulfide, 2H.

Phase ID of the XRD analysis shows that the hot acid baked treatment dissolved some copper in the chalcopyrite impurities [11], but left the iron in the MoS_2 powder. Left in samples 1-2 are cancrinite and hausmannite, and in samples, 1-3 are iron or iron phosphate, in sample 4 there is wurtzite after treatment. All of these impurities are minerals formed during or after the acid treatment.

The Pawley method was used to fit the XRD patterns of samples 1 and 3 [11], and the crystalline sizes were 86 µm and 116 µm respectively. However, since the method assumes spherical crystallites and the MoS_2 is a more flaky material the results are concluded not accurate, but a representation of the sample average. The fitting method resulted in sample 1 lattice parameters being a = 3.1652 Å, c = 12.3049 Å, and sample 3 being a = 3.1632 Å, c = 12.3019 Å. These lattice parameters show that the MoS_2 are highly crystalline, due to the parameters being similar to the MoS_2 crystal reference. The samples are determined to have too big particles for use in lithium-ion batteries as smaller crystallite sizes have better electrochemical performance.

To have a better picture of the sizes of the particles in the powder Rietveld fitting method is proposed for future work [11]. The thesis also suggests removing iron as future work before testing the MoS_2 in a coin cell for electrochemical properties. Longer time ball milling is suggested as a way of getting smaller particles to use in a lithium-ion battery. The thesis concludes that the MoS_2 from Knaben Gruver could be a good replacement for graphene in Li-ion batteries, but the material needs to be tested for electrochemical properties through coin cell testing.

2.4 Battery characteristics

Voltage capacity profiles

The voltage capacity profile of a battery is used to visualise the capacity of the cell at different voltages during the lithium (de-)intercalation reactions [34]. The profile will provide an understanding of how the cell is reacting to cycling over time. In the ideal battery, the capacity endpoint of the curves would be the same for every cycle of a test, but there will always be some loss after the first charge-discharge cycle.

Coulombic efficiency

The ratio between the charge transferred during charge and discharge is called the coulombic efficiency [35]. Due to loss of lithium during charging this number will never be 100% for a real battery. The coulombic efficiency will also indicate the battery cells' potential lifespan.

$$\mathrm{CE} = \frac{Q_{\mathrm{discharge}}}{Q_{\mathrm{charge}}} \cdot 100 \tag{4}$$

Lithium-ion batteries are dominating the rechargeable battery market in terms of coulombic efficiency with one of the highest ratings [36]. The efficiency of lithium-ion batteries in cool temperatures with not too high current can be over 99% [36].

Incremental capacity analysis

To better understand the degradation of a battery cell, the state of health can be tracked using dQ/dV analysis, or incremental capacity analysis [37]. In a curve showing cell capacity vs. voltage, the variations of voltage will indicate the variation of reactions in the cell taking place and the capacity the extent of the reaction. State of health tracking is about tracking the state of charge changes with the associated capacity and in this way interpreting the changes in composition in the cell. By plotting the derivative of the capacity over the cell voltage the graph can show the degradation of the cell chemistry over time.

The peaks of the plot will tell a story of the internal reactions of the cell [37]. The peaks of the plot can tell if the cell is losing active material or lithium ions, the cells' ohmic resistance is increasing, or if there is a new chemistry forming in the cell.

Loss of active material If the peaks are all decreasing in size, there would be a loss of active material, this could be caused by the active material losing contact with the current collector or electronically between the particles, or particle cracking [38].

Loss of lithium inventory When the plot shows the first or the last peak decreasing, it would indicate that there is a loss in lithium inventory. This could be due to lithium plating, where lithium ions get stuck as a layer preventing intercalation of lithium at this particular place in later cycling [38].

Increase of ohmic resistance The indicators of increased ohmic resistance are the peaks shifting [37]. The delithiation curve would shift towards higher voltage and the lithiation curve would shift towards lower voltages. If the metallic current collectors start to corrode the ohmic resistance would increase making the plot change.

Formation of new chemistry Cell chemistry can change during cycling, an example is the change of MoS_2 from lithium and molybdenum disulfide to lithium sulfide and molybdenum as mentioned previously [30]. If the chemistry of the cell changes this will show in the plot as the peaks change shape over time or new peaks appering[37].

2.5 Particle surface area

Cracks in the active material of an electrode can occur during charging and discharging of a cell [39]. These cracks can create more surface area for the electrolyte to electrochemically react with. Cracking of the active material could lead to capacity decay caused by side reactions in the cell.

The interface between the solid part of the electrode and the electrolyte forms a double layer [39], which acts like a capacitor. When voltage is applied, this capacitor can store or release charge by moving ions and electrons. This capacitance can be measured at different states of charge. By relating the capacitance to the electrochemical surface area, the changes in the surface area can be monitored [39] and cracks in the active material detected using a technique called electrochemical impedance spectroscopy (EIS). This can help in understanding the condition of the electrode and the integrity of the active material.

3 Experimental method

The molybdenum used in initial tests in this thesis is previously prepared and characterized in the bachelors' thesis "Preparation and Characterization of MoS_2 from Knaben Gruver in Kvinesdal for Anode Material Testing in Lithium-ion Batteries" [11]. The material was not enough to construct a battery electrode and more material was needed to be prepared. To prepare more molybdenum disulfide the same method is used, with additional research done to improve the properties of the obtained active material powder.

3.1 Preparation

3.1.1 Ball milling

The research conducted on ball milling, as referenced in the previous bachelor thesis and two research articles [40, 41], provides valuable insights into the optimal parameters for achieving successful milling results.

According to the research, the optimal mass ratio of powder to balls is recommended to be between 1:10 and 1:20 [42]. This means that for every unit of mass of powder, 10 to 20 units of mass of balls should be used in the milling process. This ratio has been found to yield desirable outcomes in terms of particle size reduction and homogeneity [40, 42].

In addition to the powder-to-balls ratio, the filling rate of the milling container is another crucial factor [42]. The research suggests that maintaining a filling rate of 30-35% of the container volume is optimal. This ensures proper tumbling and collision of the powder and balls, promoting efficient milling [42].

The research suggests that an optimal ratio falls within the range of 1.56 to 1.64. This ratio ensures sufficient milling space and proper cascading of the balls, enhancing the efficiency of particle size reduction [42].

The rotational speed of the mill is a critical parameter that significantly affects the milling process. The optimal speed is determined using the equation 5, which takes into account the critical speed. The critical speed refers to the rotational speed at which the centrifugal force holds the balls against the wall of the container. The research recommends operating the mill at 65-80% of the critical speed to achieve optimal milling results [42].

$$\mathrm{n} = \frac{42.3}{\sqrt{\mathrm{D_m}}} \cdot 0.7 \tag{5}$$

Where D_m is the diameter of the container.

Based on the experiment carried out by Harishwar Kale, Manisha Kulthe Hargude, and R. Goyal. [40] the particle sizes are decreased with increased milling time. This, and the time used in the BSc thesis [11], is the foundation of the time set for the ball milling in this experiment. The particle sizes needed for making the electrodes were smaller than those of the original powder and more preparation was therefore needed.

The molybdenum disulfide powder was put in a container and ball milled for 48 hours with all the balls mentioned in table 2. The ball milling was run three times at different powder-to-ball ratios

to find the most optimal milling and to prepare enough material for further testing. The speed was set as close to the optimal speed as possible for all the tests.

Table 2: The parts used in the three tests of powder to ceramic ball ratio of the grinding of MoS2 powder, all ground for 48 hours with all the parts mentioned.

Part	**Test 1**	**Test 2**	**Test 3**
MoS_2 before ball milling	49.97 g	32.04 g	40.06 g
D20mm	153.18 g	153.18 g	153.18 g
D10mm	85.94 g	85.94 g	85.94 g
D5mm	89.55 g	89.55 g	89.55 g
Powder to ball mass ratio	1:7	1:10	1:8

3.1.2 Hot acid baked treatment

As stated in the previous thesis the main impurities in the molybdenum disulfide from Knaben are copper iron sulfide, also called chalcopyrite. For the new sample, the same procedure of hot acid baked treatment was done.

One option to remove copper sulfides from molybdenum disulfide minerals is to dissolve them as sulfates and wash them out after treatment. This can be done with pure sulfuric acid at higher temperatures. The leaching process with sulfuric acid creates the toxic gas SO_2 if introduced to oxygen, making the process potentially hazardous.

The overall reaction of sulfuric acid and chalcopyrite at above 100 °C is as follows [43]:

$$CuFeS_{2(s)} + 4H_2SO_{4(l)} = CuSO_{4(s)} + FeSO_{4(s)} + 2SO_{2(g)} + 4H_2O_(l) \quad (6)$$

Based on the research of I. Wilkomirsky, J. Becker, and F. Parada [43] the amount of dissolved copper and iron sulfates in molybdenite increases as the temperature increases. The rate at which the copper and iron dissolves was tested at three different temperatures, 160 °C, 170 °C, and 180 °C, with the best results obtained from the 180 °C test with a reaction time of 12 hours. Figure 8 shows the overall rate at different temperatures.

The method for the treatment with sulfuric acid is described by Ikumapayi Fatai Kolawole [44] and I. Wilkomirsky, J. Becker, and F. Parada. [43], and is also based on the previous work done in [11].

The MoS_2 powder was mixed in a glass beaker with sulfuric acid to the 200 mL mark. The mixture was constantly stirred by a magnetic stirrer while being heated on a hotplate to 180 °C. Due to the forming of the toxic sulfur oxide gas, the whole procedure was done in a fume hood. The acid treatment underwent for 5 hours before the heat was turned off and the slurry cooled overnight, approximately 18 hours, with the magnetic stirrer on. The sample/acid slurry was then centrifuged 2 times for 10 min at 5500 rpm. The acid was then washed out with deionized water and centrifuged three times at the same time and rate. The samples were then dried for 24 hours in air.

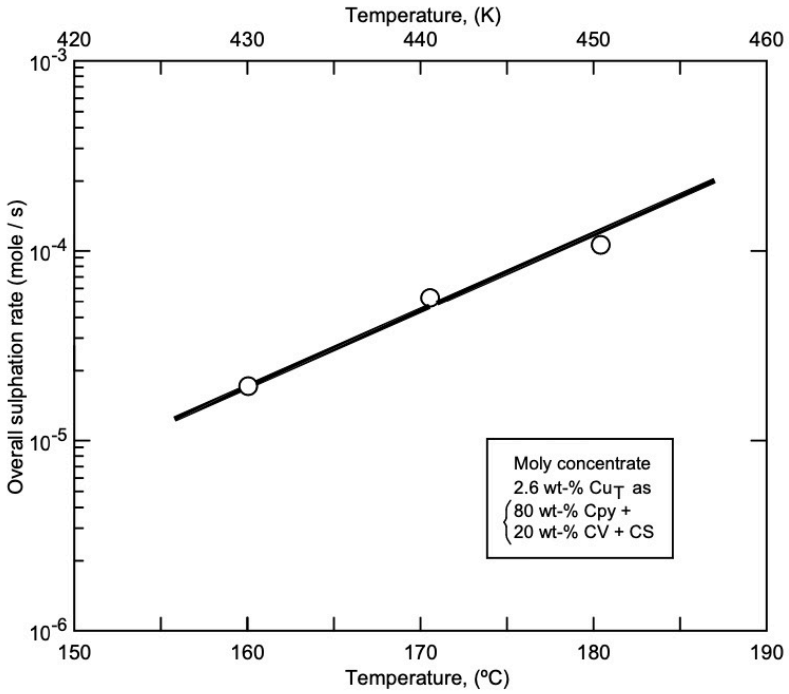

Figure 8: The curve shows how much copper is dissolved, in moles per second, in sulfuric acid at temperatures of 160, 170, and 180 °C [43], where the higher temperature gives faster dissolving.

The purified powder clumped up during the drying process after acid treatment, and milling was therefore repeated. The new parameters for ball milling can be seen in table 3. To obtain an amount of MoS_2 suitable for making anodes the powder was milled for 24 hours before sieving.

Table 3: Parameters of grinding after the MoS2 powder has been purified with sulfuric acid, the grinding was performed two times for 24 hours with two different powder-to-balls ratios.

Part	**Test 1**	**Test 2**
MoS_2 before ball milling	34.99 g	30.56 g
D20mm	153.24 g	153.18 g
D10mm	119.71 g	119.71 g
D5mm	122.14 g	122.14 g
Powder to balls ratio	1:11	1:13

3.1.3 Sieving

The molybdenum was sieved directly after ball milling for 24 hours. The sieve grid sizes were 125, 63, and 45 µms, making fractions of particle sizes above 125 µm, 125-63 µm, 63-45 µm, and below 45 µm. The vibratory sieve used was a Haver eml digital plus Test Sieve Shaker with the program being 10 minutes long with intervals of vibrations of 10 seconds on and of. The powder was carefully brushed off the sieves and put in different containers, the biggest particle sizes were ground with

mortar and pestle and sieved multiple times to obtain more samples of the smallest sizes.

3.1.4 Particle size distribution analysis

Particle size distribution (PSD) of the obtained powders was determined with a Malvern MASTERSIZER 3000 (Malvern, United Kingdom), measured through the diffraction of a laser beam through a dilute dispersion of the particles [45]. The material is put in water as a solvent and pumped through the MASTERSIZER testing chamber consisting of two glass panels. The MASTERSIZER have an ultrasound function to help dissolve the particles in the water solution and increase obscurity. Measurements of the scattered light are taken and the results can be presented as particle size histograms in the MASTERSIZER software. The smaller the particles the bigger the angle of the scattered light are. The MASTERSIZER can measure particle sizes from 10nm to 3.5 mm.

Particle size distribution analysis was done for samples milled at different conditions to measure the effect on size reduction before the acid treatment, table 4 shows all the samples tested.

Table 4: Samples were taken of the milled powder from three different tests at the times given in the "Milling duration" column of the table, the different samples were tested in the MASTERSIZER.

Test number	Milling duration / h
1	4, 8, 20, 27, 48
2	48
3	24, 48

The powder was also analyzed after removing the impurities and sieving, for the smallest particle sizes.

3.1.5 Scanning electron microscopy

Scanning electron microscopy (SEM - JEOL JSM 7200F) is used to create high-resolution images of objects with electron beams [46]. The electron beam is directed toward the sample mounted in a vacuum chamber of the microscope. The sample produces secondary electrons, backscattered electrons, and X-rays when hit with the electron beam, and detectors collect these and the images of different properties (chemical information, electrical properties, intensity of signal) of the material are automatically constructed.

To determine the content of the material a technique called Energy-dispersive X-ray spectroscopy or EDS is used [47]. The electron beam causes an electron to be ejected from the core shell of the atom, and an electron from the outer shell takes its place and emits an X-ray corresponding to the element and shell specific energy difference of the two electron states. These X-rays can be measured and the signal will tell the composition of the material being scanned. By doing a mapping with this technic the composition of an area can be determined. The results are often presented in a graph where the peaks show what element is present and the intensity of the peaks tells how much of it there is.

SEM analysis was done on the original sample prior to preparing the new material. Analysis was also

done on the new material after purification. After constructing and testing two half-cells the cells were disassembled and SEM analysis was done on two cycled electrodes to examine the electrode morphology.

3.2 Battery building and characterization

3.2.1 Coating and coin cell assembly

To construct an electrode the active material is mixed with a conductive additive and a binder. These elements together with a solvent, when mixed, are called a slurry. Carbon is often used as a conductive additive in lithium-ion batteries [48], the powder ensures that the active material is electrically connected and connected to the current collector. The binder most commonly used in electrode slurries are PVDF or polyvinylidene fluoride [49] [50]. PVDF is used because it is highly electrically stable, has little resistance and has strong adhesion. To make the powders into a paste-like slurry NMP solvent is used [51], short for N-methyl pyrrolidone. The solvent is highly effective on PVDF and is therefore used together with this binder. The slurry is coated onto a metal current collector.

The slurry for the purpose of this thesis was made using 95 wt% MoS_2 (Knaben Gruver, treated as described in section 3.1), 2 wt% carbon black (C65, Imerys Graphite and Carbon, Belgium), and 3 wt% polyvinylidene fluoride (PVDF, SOLVAY, China), the weights used are given in table 5.

Table 5: Weights and weight percents of the components of the slurry made for the electrode coatings.

Material	**Weight**	**wt%**
MoS_2	2.839 g	95
PDVF	0.09 g	3
C65	0.059 g	2

The powders were homogenized with a mixer(Mixer – Thinky ARM310, TINKY, Japan). The same amount in weight of N-methyl-2-pyrrolidone (NMP, 3 g) was then added and again mixed into a homogeneous slurry.

A copper foil was mounted to a clean glass plate and placed in a coating machine (TMAX-MS-ZN320B, 10 mm/s, 250 mm, TMAX battery equipments, China). To spread the MoS_2 slurry on the copper foil (TMAX copper foil, 15 µm x 20 mm) a gap applicator (D-58675 Hemer/Westfalen, Erichsen, Germany) with a 60 µm gap was used. The copper foil with slurry was dried at 70 °C (RCDA-1000/10S, Royal Catering, Germany) to dry completely. The same procedure was done with a 30 µm gap applicator to produce electrodes of two different thicknesses for later analysis.

Electrodes were punched out (Handheld electrode punch, Nogami, Japan) of each thickness with a 15 mm diameter size. Separators of glass fibre(glass fibre, VWR, US) with a size of 17 mm were also punched out, and pure copper plates at 15 mm were punched out to measure the average weight of the copper foil. All the components were then dried in a vacuum oven (Glass Oven B-585, BUCHI, Switzerland) for three hours at 120 °C before they were transferred to the glove box (GS Glovebox

Mega 4, Glovebox Systemtechnik, Germany).

The half-cell was constructed in an argon-filled glove box. Lithium foil (lithium foil 0.3 x 60 mm, GelonLib, China) was punched out at a 16 mm size. As an electrolyte, the cell was filled with 70 µL of 1 M LiPF6 in EC/DMC (ethylene carbonate/dimethyl carbonate) (1:1, (1M LiPF6 in EC/DMC, GelonLib, China)). Figure 9 shows the parts of the half cell, the cell was assembled by putting the parts in the cell can in the order illustrated. To determine the C-rate to cycle the cells the weight of the dried electrode was measured (MCE-Cubis II Essentials, Sartorius, Germany) before the assembly.

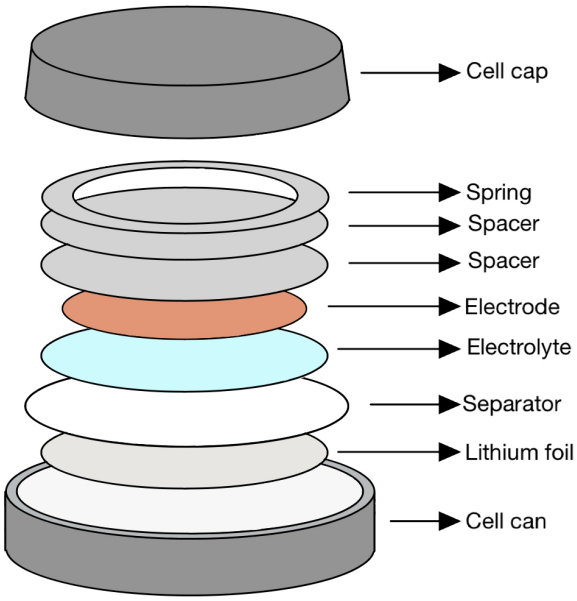

Figure 9: Illustration of the parts and order of the half-cell assembly, the electrolyte illustrated as a disk, but is, in reality, a liquid that flows in the whole cell.

3.2.2 Cycling

The cells were tested at two different C-rates, first at C/10 for three cycles. Later for C/2 for 50 cycles to determine cyclability, after 50 cycles the batteries were cycled three times at C/10. This was done from 0.2 V_{Li} - 3 V_{Li} for all cycles for one cell with 30µm coating and one with 60µm coating. The same amount of cycles was done to two similar cells but with voltages from 0.9 V_{Li} - 3 V_{Li}.

To determine the current of the test of the cells the theoretical capacity of MoS_2, 669 mAh g^{-1}, was multiplied by the mass of the active material in the cell. This was divided by the factor of the desired C-rate. The mass of the active material and the tested voltage range is given in table 6.

Table 6: The four cells tested with the coating thickness, mass of active material and the tested voltage range.

Coating thickness	Voltage range	Mass of active material	Theoretical capacity
30 µm	0.2 V_{Li}- 3 V_{Li}	3.32 mg	669 mAh g^{-1}
60 µm	0.2 V_{Li}- 3 V_{Li}	5.03 mg	669 mAh g^{-1}
30 µm	0.9 V_{Li}- 3 V_{Li}	3.60 mg	167 mAh g^{-1}
60 µm	0.9 V_{Li}- 3 V_{Li}	4.93 mg	167 mAh g^{-1}

3.2.3 Particle surface area calculations

The surface area of the electrodes in contact with electrolyte will for a double layer capacitor with electrons on the material and ions on the electrolyte side [21]. This double layer capacitance mainly depends on the electrolyte. By determining the areal double layer capacitance for the electrolyte used and then in a second step measuring the capacitance of known amounts of MoS2 material, one can estimate the surface area of the MoS2.

To first determine the areal double layer capacity in µF/cm^2 one battery cell was assembled as in figure 9 but with the electrode and lithium foil switched out with disks of copper foil with the smooth sides facing each other. One cell was also assembled with two MoS_2 electrodes facing inward. These setups are referred to as symmetric cells. The cell impedance was measured for both and used to calculate the capacitance with equation 7.

$$Z_c(\omega) = \frac{-i}{\omega \cdot C} = \frac{-i}{2 \cdot \pi \cdot f_{min} \cdot C} \rightarrow C = \frac{-i}{2 \cdot \pi \cdot f_{min} \cdot Z_c(f)} \tag{7}$$

The areal capacitance of the double layer can then be calculated with equation 8.

$$C = \varepsilon_o \cdot \varepsilon_T \cdot \frac{A}{d} \rightarrow \frac{C}{A} = \frac{\varepsilon_o \cdot \varepsilon_T}{d} \tag{8}$$

With C_1 as one copper foil or one electrode and C_2 as the other copper foil or electrode in the symmetrical cell the capacity of the whole cell can be written as C_{tot} is equal to the total capacity times two when $C_1 = C_2 = C_x$.

$$\frac{1}{C_{\text{tot}}} = \frac{1}{C_1} + \frac{1}{C_2} = \frac{2}{C_{\text{x}}} \rightarrow C_{\text{x}} = C_{\text{tot}} \cdot 2 \tag{9}$$

Given the two previous equations, the area of the copper and electrode can be calculated as in equation 10 and 11

$$\frac{C_{\text{x}}}{A_{\text{cu}}} = \frac{\varepsilon_{\text{o}} \cdot \varepsilon_{\text{T}}}{d} = \frac{C_{\text{tot,cu}}}{A_{\text{cu}}} \rightarrow A_{\text{cu}} = \frac{C_{\text{tot,cu}} \cdot 2}{\frac{\varepsilon_{\text{o}} \cdot \varepsilon_{\text{T}}}{d}} \tag{10}$$

$$\frac{C_{\text{x}}}{A_{\text{MoS}_2}} = \frac{\varepsilon_{\text{o}} \cdot \varepsilon_{\text{T}}}{d} = \frac{C_{\text{tot,MoS}_2}}{A_{\text{MoS}_2}} \rightarrow A_{\text{MoS}_2} = \frac{C_{\text{tot,MoS}_2} \cdot 2}{\frac{\varepsilon_{\text{o}} \cdot \varepsilon_{\text{T}}}{d}} \tag{11}$$

With the surface area of the two copper disks known to be 2 cm^2 (16 mm diameter disk) the now only unknown factor is the area of the particles in the MoS_2 electrode which is calculated using equation 12.

$$\frac{A_{\text{MoS}_2}}{A_{\text{cu}}} = \frac{C_{\text{tot,MoS}_2}}{C_{\text{tot,cu}}} \rightarrow A_{\text{MoS}_2} = \frac{C_{\text{tot,MoS}_2}}{C_{\text{tot,cu}}} \cdot A_{\text{cu}} \tag{12}$$

To obtain the surface area of the amount of active material in one MoS_2 cell the calculated area of the electrode is divided by the mass of the active material in the electrode measured.

4 Results and discussion

4.1 Preparation process

The first part of this thesis consists of preparing the molybdenum disulfide for battery use. The approach used is based on a top-down method and the results will be presented below.

4.1.1 Ball milling and particle size distribution analysis

To determine the effect of the ball milling samples were taken at different time intervals throughout the milling process and PSD analysis was done for each according to the time points stated in table 4 in chapter 3.1.4.

To compare the results from the previously prepared samples to the current ones, PSD was done for both raw materials at the beginning of the project. Figure 10 shows the particle distribution of the sample received in 2021 after milling for 24 hours. Figure 11 shows the PSD of the new sample obtained in 2023 after approximately 24 hours of ball milling according to the procedure described in chapters 3.1.1 and 3.1.2.

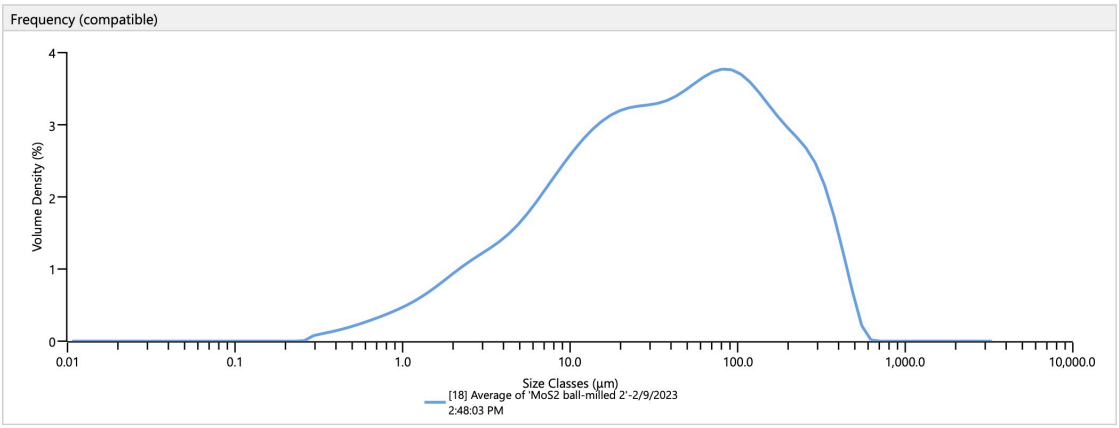

Figure 10: Particle sizes distribution of the MoS_2 powder prepared in 2021 after 24 hours of milling with ceramic balls, the PSD was recorded in 2023 from the material remaining from the 2021 study, and the main particle sizes are ranging between 10 µm and 400 µm.

In figure 11 the particles agglomerate making two peaks appear in the plot, the particles agglomerate in the water solution where the powder is solved. MoS_2 in the form of powder is hydrophobic [52], contributing to the agglomeration of particles in the water dissolvent. The MASTERSIZERs ultrasound made the obscurity of the solution higher, but the agglomeration worsened as soon as the ultrasound stopped. The peak appearing at the right in most plots of the PSD is therefore neglected in most cases.

Figures 10 and 11 show that the peak of the graph is shifted slightly towards the left for the newest sample compared to the old one when neglecting the right peak of the new sample. Meaning that the milling of the newest sample produced the smallest particles. The sample is taken from test number 3 where the ratio of powder to milling balls was 1:8, according to the previous thesis [11] this was also the ratio of the powder preparation procedure in 2021. This indicates that the speed variable could be a crucial factor in the particle size reduction, as the speed of the 2021 sample is

not given.

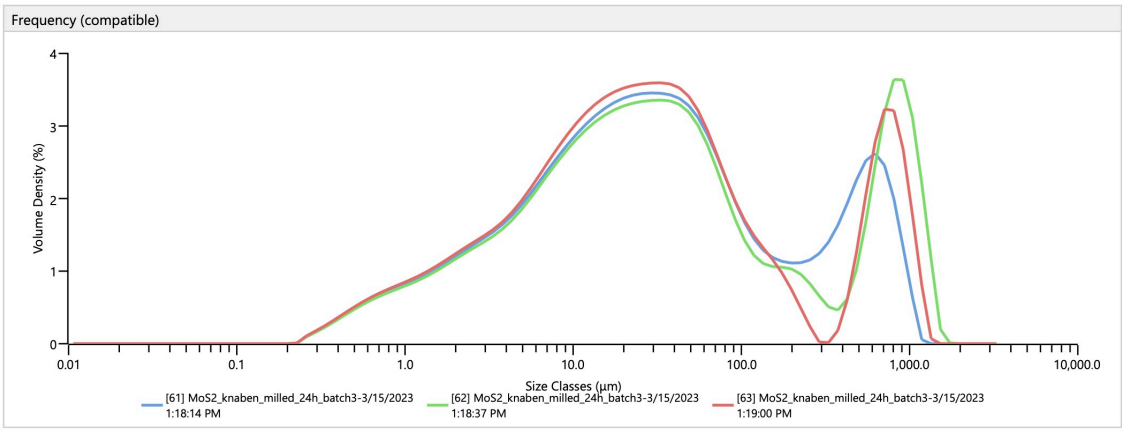

Figure 11: The particle size distribution analysis of the sample collected from Knaben Gruver in 2023, the three curves showing measurements of the same sample milled for 24 hours with main sizes between 5 µm and 100 µm.

To verify the statement by Harishwar Kale, Manisha Kulthe Hargude, and R. Goyal. [40] that the longer time milling would produce smaller particles small amounts of powder were taken out at different time intervals as shown in table 4. The samples were run through a PSD analysis and the results of the analysis are shown in figure 12.

In the graph, the peak showing the most abundant particle sizes is shifting towards the left corresponding to smaller particle sizes.

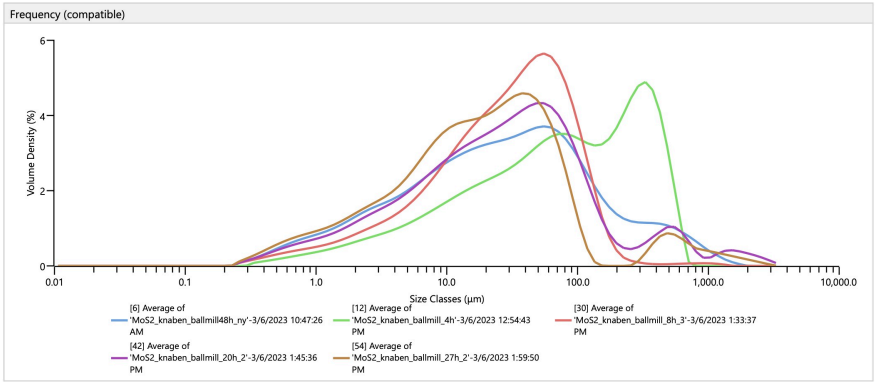

Figure 12: Particle size distribution of the MoS_2 powder milled for 4, 8, 20, 27, and 48 hours according to the procedure in table 4.

The increase in time is giving smaller particles. The exception to this is the graph showing the sample milled for 27 hours. The brown 27-hour curve is showing smaller particles than the blue 48-hours curve. This could be an agglomeration of the particles after 27 hours potentially due to heat and grinding during extensive milling.

To verify the results of the 48-hours ball milling two more tests were carried out, with different powder-to-ball ratios. The ratios are shown in table 2, and the results of changing the powder mass are shown in figure 13.

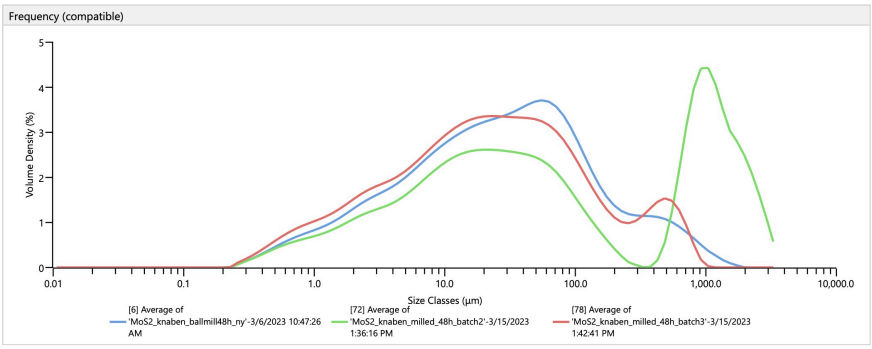

Figure 13: Measurements, measured with a Malvern MASTERSIZER 3000, of three batches of MoS_2 powder milled with the powder-to-balls ratios of 1:7, 1:10, and 1:8 for 48h.

In the first test, represented by the blue curve, a ratio of 1:7 was used. The second test, shown by the green curve, had a ratio of 1:10. Lastly, the third test, indicated by the red curve, employed a ratio of 1:8. Based on the three tests the ratio of 1:8 generally gave the largest amount of smaller particles (red curve in Figure 14).

4.1.2 Sulfuric acid purification

It is stated in the bachelor thesis that the hot acid baked treatment might be more effective on ball-milled powder [11]. Ball milling was therefore performed before treatment with sulfuric acid.

The procedure of purifying the molybdenum disulfide in 2021 is described in section 2.3.3, this procedure was modified for the experiment of this thesis. The difference between having a magnetic stirrer and doing the acid treatment on a hotplate seems to have affected the amount of impurities left. Both the 2021 powder and the current sample were analyzed with SEM after treatment. The 2023 MoS_2 powder had no traces of copper and iron left after treatment, while the 2021 powder still showed impurities.

During the acid treatment and drying the MoS_2 powder clumped up, it was therefore milled with the parameters mentioned in chapter 4.1.1. The milling was done for 24 hours before a particle size distribution analysis was done, the results are presented in figure 14.

The particle sizes after milling the purified MoS_2 are about the same as before the treatment. Most of the particles are between 19 and 40 µm, which is also seen in appendix 6.

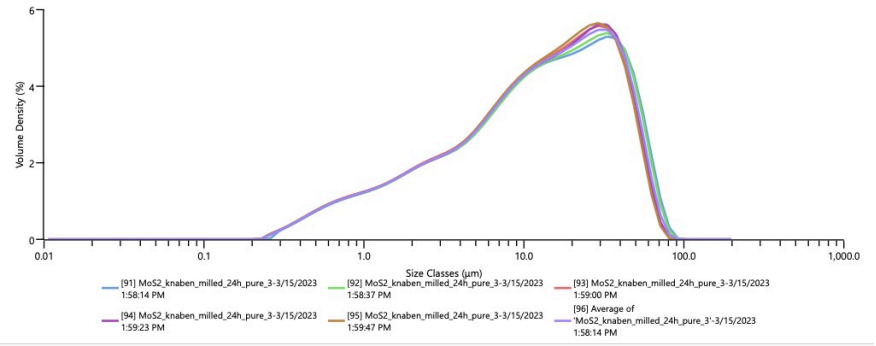

Figure 14: Five measurements of particle sizes of the same sample of purified MoS_2 after 24 hours of milling.

To obtain a particle size suitable for building an electrode the powder was sieved with different sizes of sieves. The sieving process resulted in different fractions of sizes of the molybdenum powder, which are shown in table 7. The table also shows that the amount of powder that was sieved was 63.3 g, and almost 7% of the powder was lost during the process. Powder was also lost in the process of milling with ceramic balls, both before and after purification. With the available sieves, the smallest size fraction of MoS_2 was below 45 µm, and the weight obtained with this size was 6.9 grams of powder, almost 10% of the original powder.

Table 7: Amounts of MoS2 in different particle sizes after sieving.

Fraction	**Amount**
Total amount before sieveing	63.3 g
Above 125 µm	17.5 g
125 - 63 µm	21.3 g
63 - 45 µm	13.7 g
Below 45 µm	6.9 g
Total amount after sieving	59.4 g

Compared to figure 7, where there are still traces of sodium, aluminium, silicon, iron, and copper, there are fewer impurities left in the EDS measurements of the newly prepared MoS2 from this study in figure 15. The change in treatment, from oven heating without stirring, to hotplate heating with stirring removed all impurities except aluminium and silicon. Silicon-based materials are commonly used in batteries [2] and the 3% silicon detected in the powder is therefore not considered a problem in further studies. There is also 2% aluminium showing in the EDS mapping which may be an impurity or a result of the aluminium sample holder in the SEM. In Appendix F the whole mapping of the powder is presented for the interested reader. The small traces of aluminium and silicon are of uncertain amounts due to the high uncertainty of quantitative EDS without internal references.

Figure 15 shows the molybdenum disulfide after the purification with sulfuric acid. The figure shows traces of oxygen and silicon clumped up in one spot at the top of the mapping picture, in green. The acid treatment targeted the copper and iron impurities and there are therefore silica impurities left in the powder. The mapping also shows small traces of aluminium in the area close to the silica. The dark purple that represents the carbon is the carbon tape that the sample is mounted on.

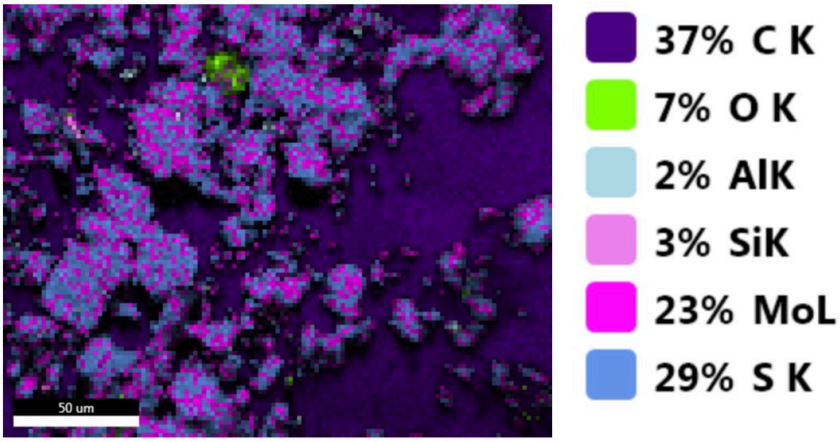

Figure 15: EDS mapping of a randomly selected area of the 2023 purified powder, the mapping show traces of Al, Si and O impurities.

Figure 16 shows the same area as the EDS mapping in figure 15. The figure shows how the MoS_2 particles are in a wide range of sizes with smaller particles on top of bigger ones. The particles are appearing as flakes laying in piles in the SEM picture. The area in which the oxygen and silicon are gathered is marked red and blue in the figure and seems to be somewhat differently structured than the rest. The area marked with a red circle is silicon and oxygen and the area marked with a blue circle is only silicon.

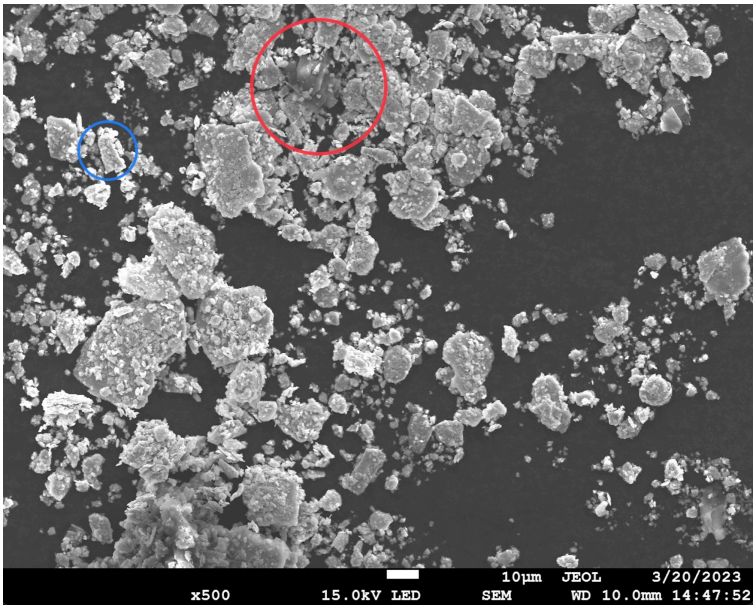

Figure 16: SEM picture of a randomly selected area of the 2023 purified powder showing different ranges of sizes of the particles from nano to micro level.

During the process of washing out the acid, the suspension turned to a greenish colour, which could mean that the molybdenum is in the semiconducting 2H phase at this point. The sample from 2021 had the same effect on the suspension when ball-milled, but the un-ball-milled sample had a brownish colour. This could mean that the ball milling made the molybdenum change phases from 1T to 2H.

The SEM analysis presented in chapter 2.3.3 also suggests that the impurities are not embedded in the MoS_2 particles, but rather lying on top of them. Breaking the copper and iron loose from the MoS_2 and into smaller pieces with milling could make the process of dissolving them faster.

4.2 Battery building and characterization

4.2.1 Cycling between 3 V_{Li} and 0.2 V_{Li}

Voltage capacity profiles

In figure 17 the first three cycles of two cells are plotted, the cell represented in figure 17a has a coating of 30 µm thickness and in figure 17b the coating is 60 µm thick. The first lithiation of the MoS_2 electrode has two plateaus, one at 1.1 V_{Li} and one at 0.6 V_{Li}. The first plateau is associated with the lithium insertion in the MoS_2 structure. The second plateau in the curve is associated with the formation of lithium-sulfur and molybdenum as described in equation 3 in chapter 2.3.2. The theoretical capacity of MoS_2 is 669.74 mAh g^{-1}, but for the first lithiation of the electrode, the capacity is higher. This could be the effect of the SEI layer forming in the first lithiation.

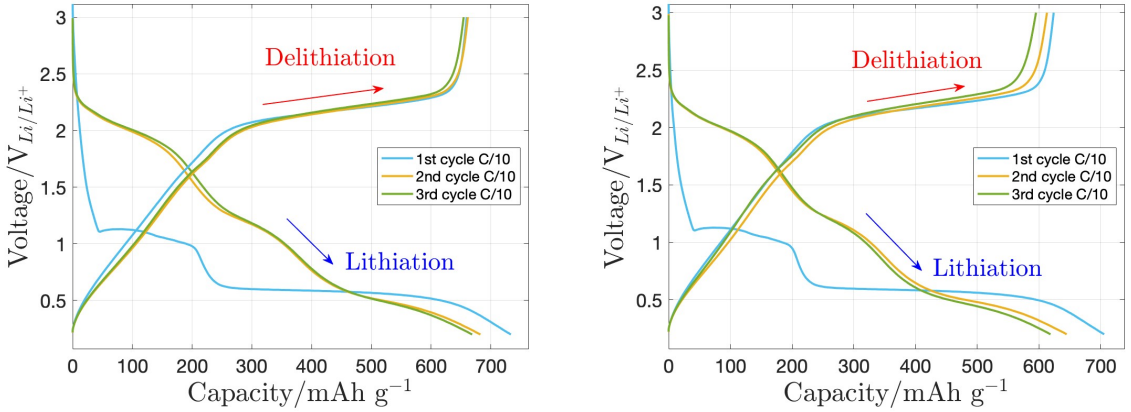

(a) 30 µm half cell

(b) 60 µm half cell

Figure 17: Voltage capacity profiles for the first three cycles of a 30 µm thickness electrode and a 60 µm thickness electrode cycled at C/10 between 3 and 0.2 V_{Li}.

The decline in capacity for the 30 µm cell is little between the 2nd and the 3rd cycle for this C-rate, but there are now three plateaus at 2.2 V_{Li}, 1.2 V_{Li}, and 0.5 V_{Li}. The 60 µm cell experiences a more rapid decline, but compared to the cycling at C/2 the cell seems to be holding better between cycles 2 and 3. The lithiation is, however showing other characteristics in the 2nd and 3rd cycles, the curve now has three plateaus instead of two, at 2.2 V_{Li}, 1.3 V_{Li} and 0.5 V_{Li}. The lithiation of the MoS_2 is now happening in three steps. The delithiation is happening mainly in one step, at 2 V_{Li}, meaning extraction of lithium ions from the structure is happening all at once.

Cycling at a lower speed gives the lithium ions more time to move into place in the structure of the active material. Since the SEM show the MoS_2 particles as a range of sizes and flaky structures the time required to intercalate the ions is longer. If the MoS_2 particles had been spherical the travelling distance and the time required would have been lowered. This could also be a contributing factor to the low capacity of the MoS_2 at higher C-rates.

The voltage/capacity profiles of the cells in figure 18 show how the MoS_2 behaves when lithiated and delithiated multiple times at different C-rates. In the figure the capacity is drastically decreasing with more cycling at C/2 (i.e. theoretical full charge/discharge in 2 h). This could indicate that the reactions in the active materials mentioned before are not 100% reversible and as the capacity goes from $\sim$ 550 mAh g^{-1} in the 10th cycle to below 50 mAh g^{-1} in the 50th cycle. The delithiation in the 51st cycle of the cells at C/10 after 50 cycles at C/2 shows that some of the capacity is restored from below 50 mAh g^{-1} to around 150 mAh g^{-1}, but fades again after the first cycle. With the lithiation at C/10, the capacity seems to increase from the 51st to the 53rd cycle, which could be due to solid lithium deposits in the active material.

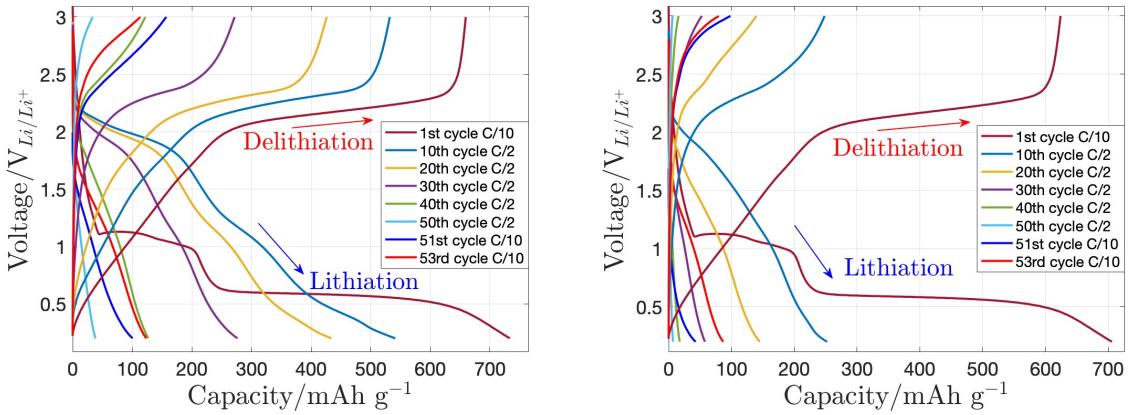

(a) 30 µm half cell

(b) 60 µm half cell

Figure 18: Voltage capacity profiles of two half cells, with 30 and 60 µm thickness electrodes, cycled at C/10 and C/2 between 3 and 0.2 V_{Li}.

The mechanisms mentioned above in the initial lithiation of the 30 µm cell seem to be happening for the 60 µm cell as well. In figure 18b the initial lithiation has two plateaus at 1.1 V_{Li} and 0.6 V_{Li} indicating the same stages of lithiation as mentioned before. The difference when cycling the thicker electrode at a faster rate is the decline in capacity, the 60 µm cell is experiencing a more rapid decline in capacity. The apparent recovery effect of the cell when cycled at lower rates after the 50 cycles at C/2 is also less pronounced.

Discharge capacity

Figure 19 compares the discharge capacities of the 30 and 60 µm cells. The decline in capacity for the 60 µm cell is happening from the 1st cycle of C/2 where it decreases with almost 100 mAh g^{-1}, from 500 to 400 mAh g^{-1}, in two cycles. The 30 µm cell has a slower capacity reduction where it takes about 20 cycles to reach a capacity of 400 mAh g^{-1}. Since the 60 µm cell is double the thickness of the coating the lithium ions have to travel to be intercalated in the active material and are also experiencing a rapid decline in capacity at a faster charging/discharging. In the figure the

capacity increases from almost 0 at C/2 to about 100 mAh g^{-1} at the last C/10 cycling. There seem to be more particles accessible at lower C-rates, increasing the capacity.

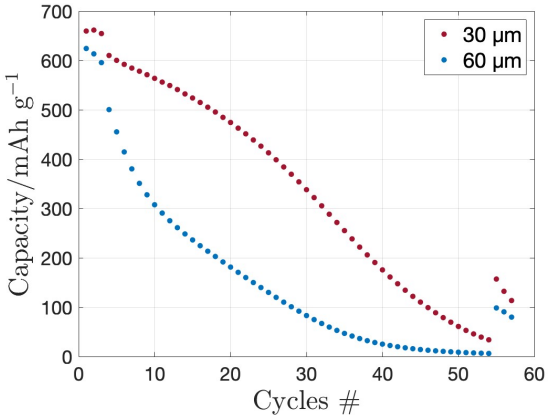

Figure 19: Discharge capacity of a 30 µm thickness electrode and a 60 µm thickness electrode showing how the capacity is fading over time when cycled between 3 and 0.2 V.

Coulombic efficiency

The coulombic efficiency of the two cells over the cycles done are shown in figure 20. The efficiency of both cells stay within 89% to 98%, but there is a rapid decline after 20 cycles for the 60 µm cell as seen in figure 20b. A battery of 98% CE would reach below 50% of its initial capacity before cycle 50 which would not be sufficient for a commercial battery.

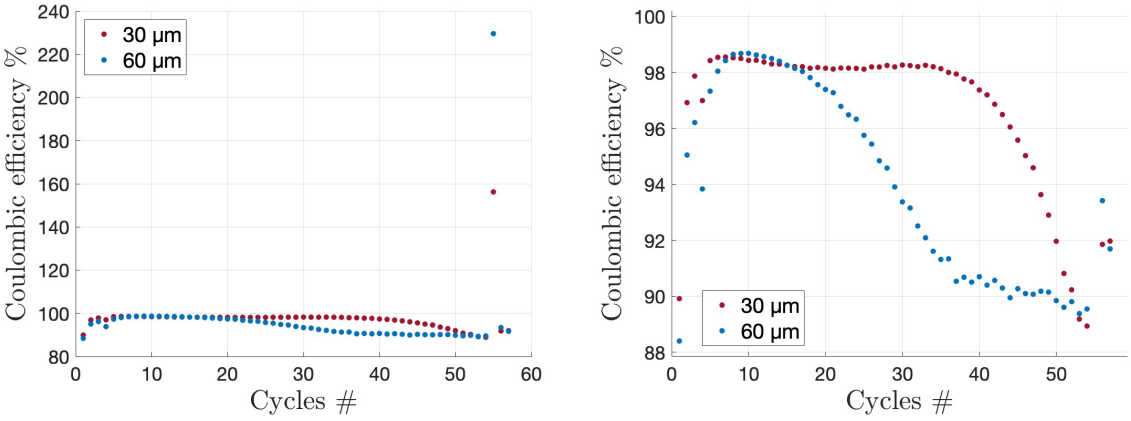

(a) 30 µm half cell

(b) 60 µm half cell

Figure 20: Coulombic efficiency of two electrodes with 30 and 60 µm thickness cycled between 3 and 0.2 V_{Li}, the left one showing two jumps in CE when cycled at C/10 and the right one showing the trend of the CE without the jumps.

The efficiency drops from above 98% to below 90% from cycle 20 to cycle 35 but seems to stabilize somewhat between cycle 35 and 50. Also, the coulombic efficiency is restored a little when cycled at C/10.

In figure 20a the coulombic efficiency jumps to over 200% for the 60 µm cell and over 140% for the 30 µm cell at the first cycle with C/10 after cycles at C/2. This could be due to less lithium

being enabled during fast charging, but more ions having the possibility to intercalate in the active material at slower charging/discharging rates.

Incremental capacity analysis

The incremental capacity analysis in figure 21 shows how the two cells are reacting to the faster charging. In the first figure, 21a, the peak of the delithiation at 2.2 V_{Li} are shifting and decreasing. The most rapid change is happening between the 30th and 40th cycle where the graph is declining to the point where there is only one peak left. The change in appearance is correlated with the loss of active material, meaning that the electrode might lose electric contact with the current collector. The shift of the peaks towards a higher voltage could indicate that there is a formation of new chemistry. The chemical reaction mentioned in previous chapters where MoS_2 and lithium go to Mo and Li_2S could explain the change in chemistry.

For the lithiation of the cell, there are three peaks that stand out, at 0.5 V_{Li}, 1.1 V_{Li} and 2 V_{Li}, these are related to the plateaus mentioned in the start of chapter 4.2.1 in relation to figures 17 and 18. For the first 20 cycles, the peak at 2 V_{Li} stays the same, but by the time of the 50th cycle, the dQ/dV line is almost flat, meaning the composition of the active material is changed. Both the cells are decomposing by the time they are cycled for the 50th time, but the process is faster for the 60 µm cell as seen in the figure. The thicker cells decomposing could be due to more side reactions in the active material.

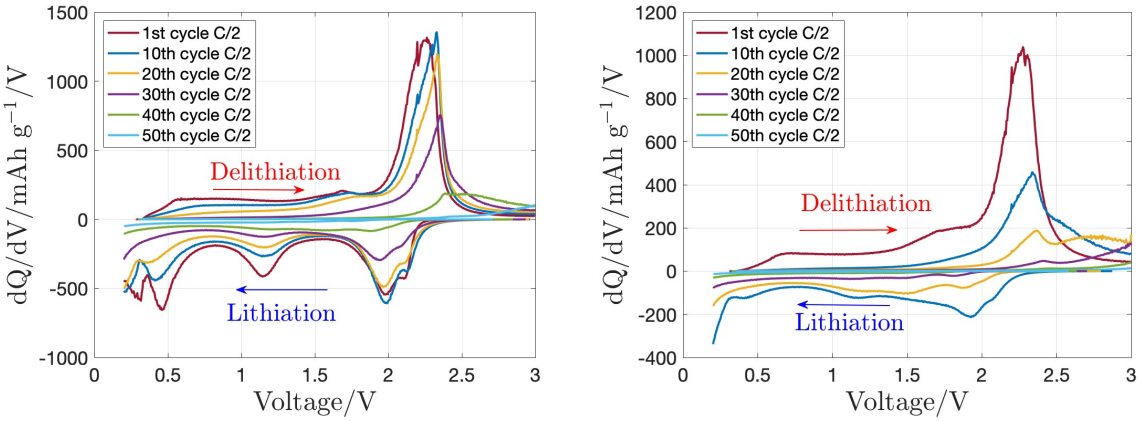

(a) 30 µm half cell

(b) 60 µm half cell

Figure 21: Incremental capacity analysis of two half cells, one at 30 µm and one at 60 µm thickness over the course of 50 cycles at C/2 between 3 and 0.2 V_{Li}, the 1st cycle of the 60 µm electrode is missing due to insufficient data.

SEM of the electrodes after cycling

After being cycled between 3 V_{Li} and 0.2 V_{Li} the two half cells were decrimped and the electrodes were taken out to be washed. The electrode was washed by soaking in the same electrolyte as inside the cell, 1:1 EC/DMC. The pictures in figure 22 are taken of the two electrodes. The thin fibres in both pictures are from the glass fibre separator in the cell. In figure 22b there are cracks in the coating, cracks are also visible in figure 22a but not to the same extent. The particle cracking can cause loss of electrical contact and cause more side reactions due to increased surface area [39] The flaky structure of the MoS_2 is now not as visible as in figure 16 of the powder before use in a coating and the particles seem to be smaller than originally. The change in particle size could be the visual effect of the loss of active material as described in chapter 4.2.1 under part "Incremental capacity analysis".

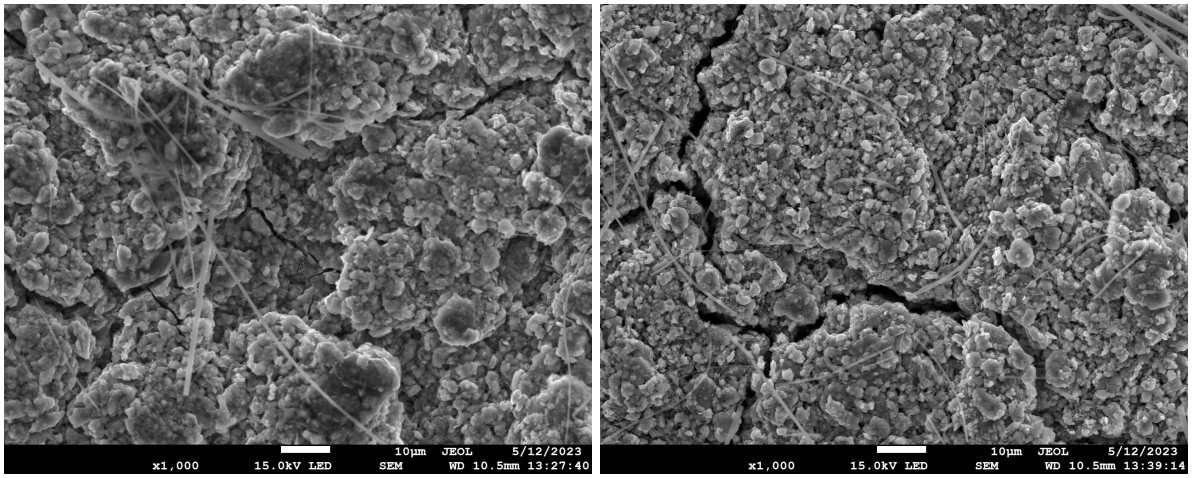

(a) 30 µm thick electrode (b) 60 µm thick electrode

Figure 22: SEM analysis of one 30 µm thick electrode(left) and one 60 µm tick electrode(right), after being cycled 56 times at C/10 and C/2 between 3 V and 0.2 V_{Li}.

4.2.2 Cycling between 3 V_{Li} and 0.9 V_{Li}

The second test of the MoS_2 electrodes is done between 3 and 0.9 V_{Li} to avoid the last part of the active material change. The following results show how the electrode behaves when cycled with the same procedure as the first tests (chapter 4.2.1) but with a different discharge setting.

Voltage capacity profiles

The voltage capacity profiles of the second test are shown in figure 24. Compared to the first test where the cells were discharged to 0.2 V, these cells are showing less degradation in capacity over time. For the 30 µm cell, the decrease seems to stop around two-thirds of the initial capacity at 160 mAh g^{-1}. And there is now only one plateau visible at 1.1 V_{Li} for the initial lithiation of the electrode, this is associated with the insertion of lithium ions in the MoS_2 layers as in equation 2 that yields 167 mAh g^{-1}.

The lithiation of the cells has two plateaus, one at 2.5 V_{Li} and one at 1.9 V_{Li} which are both at higher voltages than the cells in chapter 4.2.1. Where the previous test had only one plateau the delithiation of these cells shows two plateaus at 1.8 V_{Li} and 2.4 V_{Li}.

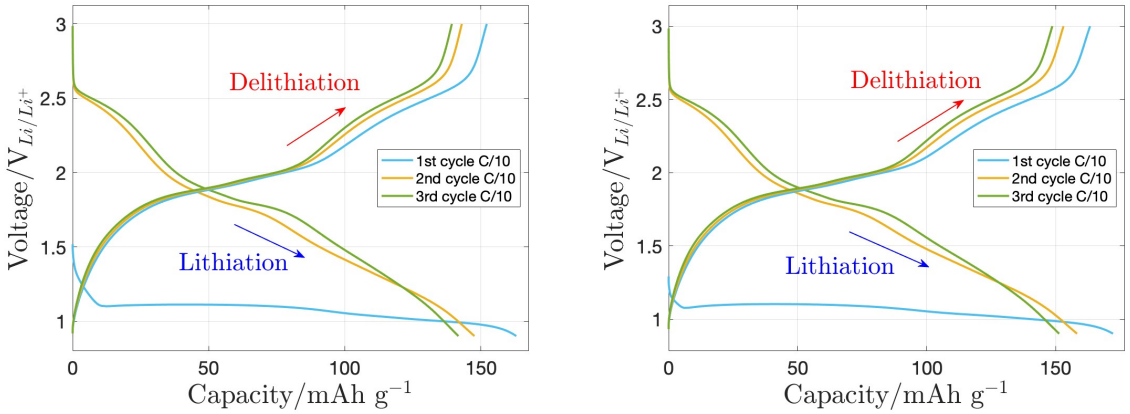

(a) 30 µm half cell (b) 60 µm half cell

Figure 23: Voltage capacity profiles for the first 3 cycles of the cell testing at C/10 for both 30 µm thickness electrode(left) and 60 µm thickness(right) cycled between 3 and 0.8 V_{Li}.

Compared to the cycling in chapter 4.2.1 the cells discharged to 0.9 V_{Li} show less decrease in capacity over the course of 50 cycles at C/2. The decrease from the first to the 50th cycle of C/10 is less than 20 mAh g^{-1} for the 30 µm cell and 50 mAh g^{-1}. this is a decrease of about 12% and 30% respectively.

After the 50 cycles with C/2 C-rate, the capacity increases when cycling at C/10. The increase in capacity for this test's voltage level is more significant than for the previous test with the lower cutoff voltage being 0.9 V_{Li} instead of 0.2 V_{Li} here. In the delithiation of the electrode, there are two plateaus appearing, one at 1.9 V_{Li} and one at 2.6 V_{Li}, these plateaus are more defined for the 30 µm cell than for the 60 µm cell.

Compared to the earlier presented studies of MoS_2 nanostructures presented by Farabi Bozheyev et al. [31] the characteristics of the lithiation within these voltages are quite similar.

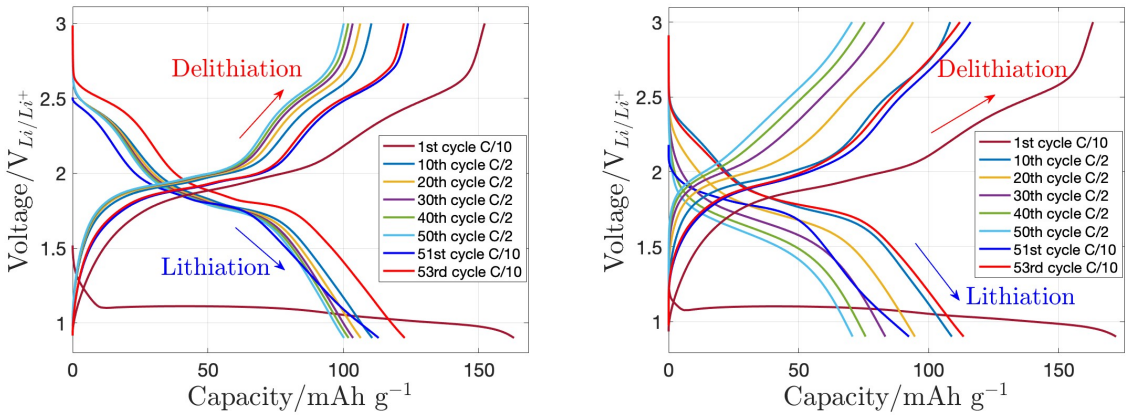

(a) 30 µm half cell (b) 60 µm half cell

Figure 24: Selected voltage capacity profiles of one electrode with 30 µm thickness coating(left) and one electrode with 60 µm coating(right) cycled 3 times at C/10, 50 times at C/2 and 3 more at C/10 between 3 and 0.9 V_{Li}.

Discharge capacity

The discharge capacity of the two cells is shown in figure 25. The capacity of the first 10 cycles of the test shows a rapid decline, from around 160 mAh g^{-1} to below 120 mAh g^{-1} for both cells. The capacity of the thinnest electrode flattens out after being cycled which might indicate that the material stabilises after some time. The thickest electrode, however, does decline further after 10 cycles. Both electrodes experience an increase in capacity when again being cycled at C/10.

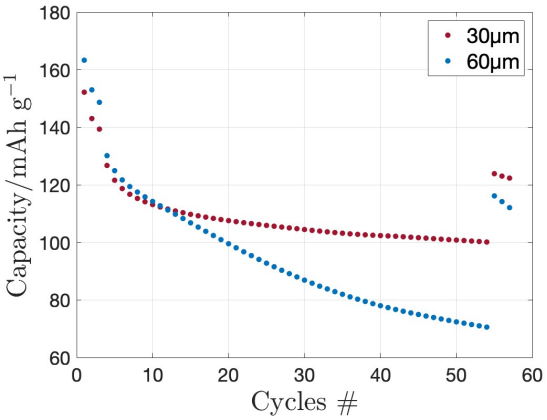

Figure 25: Discharge capacity of a 30 µm thickness electrode and a 60 µm thickness electrode showing how the capacity is fading over time when cycled between 3 and 0.9 V_{Li}.

Coulombic efficiency

The CE presented in figure 26 shows the behaviour of the two cells over the 56 cycles done in total. CE increases after the initial cycle and stabilises at 99.9% for the 30 µm cell and 99.7% for the 60 µm cell, which is better than the first test. The cell of 99.9% CE would last for about 700 cycles before reaching 50% of initial capacity and the cell of 99.7% would last around 250 cycles. This is much better than the cells with deeper discharge, but would due to the low theoretical capacity not be a good candidate to replace graphite.

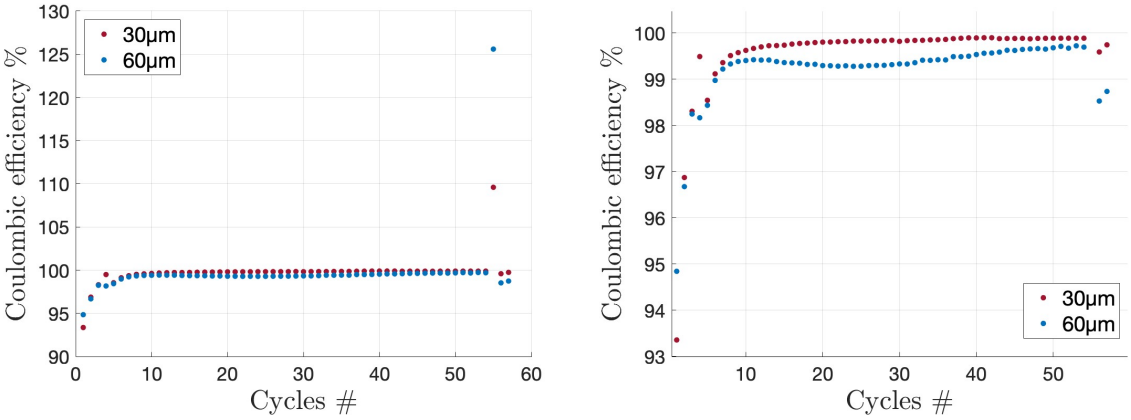

(a) 30 µm half cell

(b) 60 µm half cell

Figure 26: Coulombic efficiency of two electrodes with 30 and 60 µm thickness cycled between 3 and 0.9 V_{Li}, the left one showing two jumps in CE when cycled at C/10 and the right one showing the trend of the CE without the jumps.

As in the full voltage window test described in chapter 4.2.1, there is an apparent recovery effect of the efficiency in the 54th cycle (1st C/10 cycle after C/2 cycling). This could be inaccessible capacity due to range limitations at higher currents such as resistances, diffusion limitations or poor electrical contacts. This will lead to a higher discharge capacity and a higher CE. The efficiency decreases after the jump to below the stabilised point but starts to increase after the C/10 cycle.

Incremental capacity analysis

The dQ/dV analysis in figure 27 shows a very different result than in the first test. Figure 27a with the results for the 30 µm cell shows only significant changes from the first cycle to the rest of the test. There is a change in peak shape from the initial delithiation to the rest, indicating a change in the active material after the first cycle. The change could be associated with the previously mentioned phase shift of the MoS_2 structure during lithiation.

The 60 µm cell shows more degradation when cycled, however, the peaks are not destroyed as for the first cell testing. This cell shows signs of loss of active material and new chemistry forming. Throughout the cycling of the cell, the peaks are all decreasing in size and changing shape. The most drastic change is happening between the first and the tenth cycle of the delithiation, this curve is similar for the two cells in the second test.

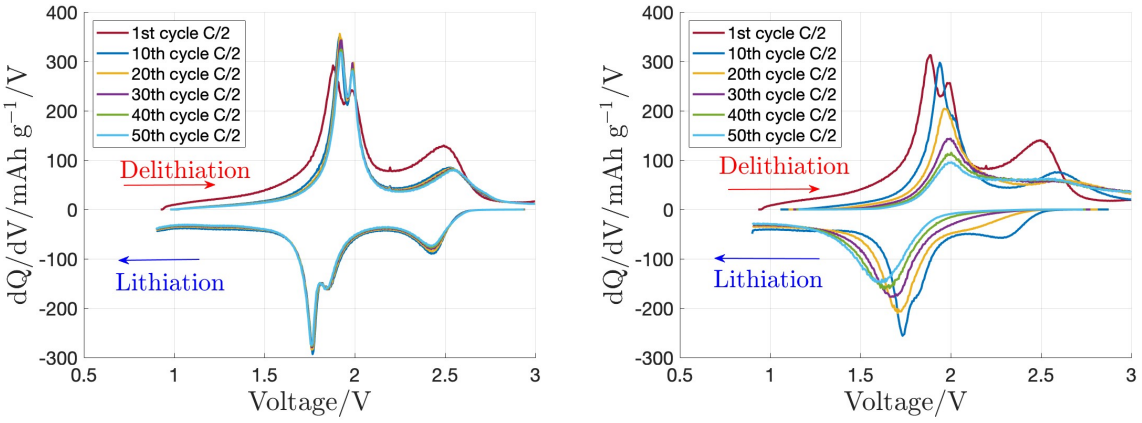

(a) 30 µm half cell

(b) 60 µm half cell

Figure 27: Incremental capacity analysis of two half cells, one at 30 µm and one at 60 µm thickness throughout 50 cycles at C/2 between 3 and 0.9 V_{Li}.

4.3 Particle surface area

With the calculations in chapter 3.2.3 the capacitance of the electrolyte in the copper cell and the MoS_2 electrode was calculated.

$$C_{MoS_2} = \frac{1}{2 \cdot \pi \cdot f_{min} \cdot Z_c(\omega)} = \frac{1}{2 \cdot \pi \cdot 0.1\text{Hz} \cdot 479\Omega} = 3.32 \cdot 10^{-3}\text{F} = 3.32\text{mF}$$

$$C_{Cu} = \frac{1}{2 \cdot \pi \cdot f_{min} \cdot Z_c(\omega)} = \frac{1}{2 \cdot \pi \cdot 0.65\text{Hz} \cdot 199998\Omega} = 1.22 \cdot 10^{-6}\text{F} = 1.22\mu\text{F}$$

With equation 12 and the mass of the active material the surface area of MoS_2 per gram is calculated.

$$A_{MoS_2} = \frac{C_{tot,MoS_2}}{C_{tot,cu}} \cdot A_{cu} = A_{MoS_2} = \frac{3.32 \cdot 10^{-3}\text{F}}{1.22 \cdot 10^{-6}\text{F}} \cdot 2 \cdot 2\text{cm}^2 = \frac{5461\text{cm}^2}{0.0036\text{g}} = 19.66\text{cm}^2\text{g}^{-1}$$

Using the calculations in chapter 3.2.3, the average surface area of the particles in the electrode is calculated to be 19.66 cm^2 g^-1 for 3.6 mg of MoS_2 in the electrode. This would be only an estimate

of the average of the surface area as the particles of the MoS_2 powder are of various sizes as seen in the SEM in figure 16.

The calculated surface area of the particles in the MoS_2 coating is larger than that of commercial graphite, which would affect the performance of the electrode. With a larger surface area, the electrode will have more side reactions resulting in the degradation of the electrode. As the 60 µm cell degrades faster than the 30 µm cell there might be more side reactions happening.

5 Conclusions

The problem mentioned in chapter 1 was if the natural MoS_2 mined at Knaben Gruver could be used as anode material in lithium ion batteries. This thesis investigated the electrochemical properties of MoS_2 powder in lithium-ion batteries with a top-down preparation process. The preparation process involving chemical purification, grinding with ceramic balls and sieving has effectively made the MoS_2 particles smaller than the original.

An EDS mapping found that the main parts of the powder received from Knaben were molybdenum and sulfur, with very small traces of silicon, aluminium, and oxygen. The milling of the powder and sieving obtained particles mostly in a size range between 19 and 40 µm, making it possible to electrochemically test the material as active material in a half cell.

The four electrodes were assembled in coin cells with lithium as reference/counter electrode, two with 60 µm thickness coating and two with 30 µm thickness coating. Two cells, one of each coating thickness, were tested between 3 V_{Li} and 0.2 V_{Li}. The first lithiation of these cells shows two plateaus, the first plateau is associated with the intercalation of lithium ions in the MoS_2 layers. The second plateau is associated with $LiMoS_2$ dissolving further into 2 Li_2S and Mo yielding the theoretical capacity of 669 mAh g^{-1}. The discharge to 0.2 V_{Li} at C/2, however, causes the active material in the electrode to decay. Both the cells decrease in capacity to almost zero over the course of 50 cycles of C/2, the thicker electrode decrease almost ten times as fast as the thinner one for the first cycles at C/2. The dQ/dV analysis of the two electrodes shows a rapid and severe change in the material of the two cells, with both loss of active material and an increase in ionic resistance. The thicker electrode seems to decay at a faster rate and the SEM picture of the two electrodes confirms that the thickest electrode visually has had the biggest change in material with particles smaller in size and large cracks in the surface. The calculations of the average surface area of the particles in the electrodes also show that the particles have large surface areas which will contribute to side reactions happening.

The two other cells assembled were cycled between 3 V_{Li} and 0.9 V_{Li} to avoid the last chemical reaction. This reaction only yields the theoretical capacity of 167 mAh g^{-1} because of the reaction where one lithium ion intercalates in the MoS_2 layers, which the test shows. The first lithiation of the cell now has only one plateau, at 1.1 V_{Li}. The cycling of these cells shows much less decay of the cell and the capacity decreases to 60% of the first lithiation, whereas the in the first test the capacity decreases to below 10% of the first lithiation. The discharge capacity seems to stabilise at around 100 mAh g^{-1} for the 30 µm cell but further decreases down to 70 mAh g^{-1} when cycling at C/2. The dQ/dV analysis of the two cells shows that the 30 µm cell only changes from the first cycle to the rest, meaning that the cell chemistry is not altered with cycling as for the other cells. The 60 µm cell seems to have some chemistry changes and more ionic resistance increase, but not as much as the cell discharges to 0.2 V_{Li}. All the cells that were tested showed a higher capacity in the initial lithiation, which could be due to the SEI layer forming in this first cycle.

The tests executed in this experiment did not yield as much capacity as the studies of MoS_2 nanostructures, but it made it possible to characterize the powder as an anode in a half cell. Optimizing the used techniques has made the particles of MoS_2 effectively smaller in size. But the ball-milling is nowhere near making the MoS_2 applicable in batteries in the same way as other more expensive methods. The bulk MoS_2 are not showing the same promise as an anode material as

single layered MoS_2 synthesized by hydrothermal synthesis, exfoliation, CVD etc.

6 Future work

Further research on natural MoS_2 is needed to make the material reach its full potential in lithium ion batteries. The powder used for testing in this thesis showed some impurities left of silicon, oxygen and aluminium, these numbers are low with only a few percentages of each, but removing especially the aluminium could have an effect on the battery performance and could be looked into.

The length that the lithium ions have to travel in the active material in the electrode will have an impact on performance. As the particles found in this thesis were of various sizes and shapes the particle sizes could also be improved and other methods of making the MoS_2 smaller could be looked into for enhanced performance.

The three research articles mentioned in this thesis have shown that MoS_2 can yield a greater capacity than graphite and the prepared material in this study. As an extension of this work, it would be interesting to look at the method of coating the MoS_2 from Knaben with silicon or other materials to help the layered structure to better keep its properties when lithiated and delithiated.

For this thesis an SEM and EDS analysis of an unused electrode was also planned to compare with the surface area of the used electrodes. But as the SEM was not available for some time during the work period this was never done. To get a better understanding of the differences between before and after cycling of the MoS_2 electrode this could be done at another time.

The surface area calculations gave a rough estimate of the average surface area of the particles in the electrode, but a BET analysis could give a better understanding of the particles in the MoS_2 powder.

Bibliography

[1] Hiroshi Kawamura et al. "FRONTIER TECHNOLOGY ISSUES LITHIUM-ION BATTERIES: A PILLAR FOR A FOSSIL FUEL-FREE ECONOMY?" In: *United Nations economic analysis* (), pp. 1–10. DOI: https://www.un.org/development/desa/dpad/wp-content/uploads/sites/45/publication/FTI_July2021.pdf.

[2] Amit Mishra et al. "Electrode materials for lithium-ion batteries". In: *Materials science for energy technologies* 1.2 (2018), pp. 182–187. DOI: https://doi.org/10.1016/j.mset.2018.08.001.

[3] Becky Chapman. *How does a lithium-ion battery work?* URL: https://letstalkscience.ca/educational-resources/stem-in-context/how-does-a-lithium-ion-battery-work. (accessed: 30.05.2023).

[4] Casey Crownhart. *What's next for batteries.* URL: https://www.technologyreview.com/2023/01/04/1066141/whats-next-for-batteries/. (accessed: 29.05.2023).

[5] Hao Zhang et al. "Graphite as anode materials: Fundamental mechanism, recent progress and advances". In: *Energy storage materials* 36 (2021), pp. 147–170. DOI: https://doi.org/10.1016/j.ensm.2020.12.027.

[6] Roland Fivaz and Etta Mooser. "Mobility of Charge Carriers in Semiconducting Layer Structures". In: *Physical Review* 163 (1967), pp. 743–755. DOI: 10.1103/PHYSREV.163.743.

[7] Helmut Tributsch and J. Craig Bennett. "Electrochemistry and photochemistry of MoS2 layer crystals. I". In: *Journal of Electroanalytical Chemistry* 81 (1977), pp. 97–111. DOI: 10.1016/S0022-0728(77)80363-X.

[8] Feipeng Yang et al. "MoS_2 for beyond lithium-ion batteries". In: *APL Energy* 9.5 (2021). DOI: https://doi.org/10.1063/5.0050118.

[9] Andreas Sigersvold. "Notat kjemisk rensing av molybden disulfid konsentrat". Notat på MoS2 prøve sendt fra Knaben Gruver. 2021.

[10] knaben.no. *Knabens historie.* URL: https://knaben.no/knabens-historie/. (accessed: 03.06.2023).

[11] Christopher Sebastian Pereira. "Preparation and Characterization of MoS2 from Knaben Gruver in Kvinesdal for Anode Material Testing in Lithium-ion Batteries". Bacheloroppgave. UiA, Universitetet i Agder, 2021, pp. 1–80.

[12] Junxiong Wu, Francesco Ciucci, and Jang-Kyo Kim. "Molybdenum Disulfide Based Nanomaterials for Rechargeable Batteries". In: *Chemistry—A European Journal* 26.29 (2020), pp. 6296–6319. DOI: https://doi.org/10.1002/chem.201905524.

[13] Scott minos. *How lithium-ion batteries work.* URL: https://www.energy.gov/energysaver/articles/how-lithium-ion-batteries-work. (accessed: 15.05.2023).

[14] Gregory L. Plett. *Battery Management Systems vol. 1: battery modeling.* battery management systems. Artech house, 2015. ISBN: 978-1-63081-023-8.

[15] onecharge.biz. *Types of lithium batteries:lithium cell chemistry.* URL: https://www.onecharge.biz/lithium-cell-chemistry/. (accessed: 30.05.2023).

[16] Battery University. *BU-306: What is the function of the separator?* URL: https://batteryuniversity.com/article/bu-306-what-is-the-function-of-the-separator. (accessed: 30.05.2023).

[17] Aiping Wang et al. "Review on modeling of the anode solid electrolyte interphase (SEI) for lithium-ion batteries". In: *npj Computational Materials* 4.15 (2018). DOI: https://doi.org/10.1038/s41524-018-0064-0.

[18] Battery University. *BU-307: How does electrolyte work.* URL: https://batteryuniversity.com/article/bu-307-how-does-electrolyte-work. (accessed: 30.05.2023).

[19] Battery University. *BU-204: How do lithium batteries work.* URL: https://batteryuniversity.com/article/bu-204-how-do-lithium-batteries-work. (accessed: 30.05.2023).

[20] Ben Rowden and Nuria Garcia-Araez. "Estimating lithium-ion battery behavior from half-cell data". In: *Energy reports* 7.2 (2021), pp. 97–103. DOI: https://doi.org/10.1016/j.egyr.2021.02.048.

[21] R Siburian et al. "Performance of graphite and graphene as electrodes in primary cell battery". In: *Journal of physics: Conferense series* 1116.4 (2018), pp. 1–7. DOI: 10.1088/1742-6596/1116/4/042034.

[22] Myounggu Park et al. "A review of conduction phenomena in Li-ion batteries". In: *Journal of Power sources* 195.24 (2010), pp. 7904–7929. DOI: https://doi.org/10.1016/j.jpowsour.2010.06.060.

[23] Wen Qi et al. "Nanostructured anode materials for lithium-ion batteries: Principle, recent progress and future perspectivesy". In: *Journal of Materials Chemistry* 5 (2017). DOI: 10.1039/C7TA05283A.

[24] Anand Bhatt, Ray Withers, and Guoxiu Wang. *Lithium-ion batteries.* URL: https://www.science.org.au/curious/technology-future/lithium-ion-batteries. (accessed: 04.06.2023).

[25] American chemistry society. *Molybdenum disulfide.* URL: https://www.acs.org/molecule-of-the-week/archive/m/molybdenum-disulfide.html. (accessed: 07.05.2023).

[26] Haibo Shu et al. "Capacity fading mechanism and improvement of cycling stability in MoS2-based anode materials for lithium ion Batteries". In: *Nanoscale* 8 (2016), pp. 2918–2926. DOI: https://doi.org/10.1039/C5NR07909H.

[27] Bimal Raut. *synthesis on nanomaterials: bottom-up and top-down approach.* URL: https://chemistnotes.com/nanochemistry/synthesis-of-nanomaterials-bottom-up-and-top-down-approach/. (accessed: 13.05.2023).

[28] Lucky Li. *Application of PVP dispersant in lithium battery industry.* URL: https://www.takomabattery.com/application-of-pvp-dispersant-in-lithium-battery-industry/. (accessed: 30.05.2023).

[29] Liang Zhang et al. "Electrochemical Reaction Mechanism of the MoS2 electrode in a Lithium-Ion Cell revealed by in situ and operando X-ray Absorption Spectroscopy". In: *Nano Letters* 18 (2018). DOI: 10.1021/acs.nanolett.7b05246.

[30] Qingmei Su et al. "Direct Studies on the Lithium- Storage Mechanism of Molybdenum Disulfide". In: *Scientific reports* 7 (2017). DOI: 10.1038/s41598-017-07648-0.

[31] Farabi Bozheyev et al. "MoS2 nanopowder as anode material for lithium-ion batteries produced by self-propagating high-temperature synthesis". In: *Materials today: proceedings* 4.3 (2017), pp. 4567–4571. DOI: https://doi.org/10.1016/j.matpr.2017.04.031.

[32] Xuan Wei et al. "Three-dimensional hierarchically porous MoS2 foam as high-rate and stable lithium-ion battery anode". In: *nature communications* 13.6006 (2022), pp. 1–12. DOI: https://doi.org/10.1038/s41467-022-33790-z.

[33] Jun-Seob Park et al. "Silicon-protected, vertically grown MoS2 nanosheets for high-performance thin-film Li-ion batteries". In: *Ceramics international* 49.3 (2023), pp. 5538–5542. DOI: https://doi.org/10.1016/j.ceramint.2022.11.200.

[34] BioLogic.com. *How to read battery cycling curves*. URL: https://www.biologic.net/topics/how-to-read-cycling-curves/. (accessed: 23.05.2023).

[35] quantumspace.com. *Coulombic efficiency demystified*. URL: https://www.quantumscape.com/resources/blog/coulombic-efficiency-demystified/. (accessed: 26.05.2023).

[36] Battery university. *BU-808c: Coulombic and energy efficiency with the battery*. URL: https://batteryuniversity.com/article/bu-808c-coulombic-and-energy-efficiency-with-the-battery. (accessed: 15.05.2023).

[37] Matthieu Dubarry, Arnaud Devie, and Bor Yann Liaw. "The value of battery diagnostics and prognostics". In: *Journal of Energy and Power Sources* 1.5 (2014), pp. 242–249. DOI: https://www.researchgate.net/publication/272170200.

[38] Christoph R. Birkl et al. "Degradation diagnostics for lithium ion cells". In: *Journal of Power Sources* 341.1 (2017), pp. 373–386. DOI: https://doi.org/10.1016/j.jpowsour.2016.12.011.

[39] Stefan Oswald et al. "Novel Method for Monitoring the Electrochemical Capacitance by In Situ Impedance Spectroscopy as Indicator for Particle Cracking of Nickel-Rich NCMs: Part I. Theory and Validation". In: *Journal of the Electrochemical Society* 167 (2020). DOI: 10.1149/1945-7111/ab9187.

[40] Harishwar Kale, Manisha Kulthe Hargude, and R. Goyal. "Synthesis of Molybdenum Disulfide (MoS2) Nanopowder Using Planetary Ball Mill". In: Feb. 2016.

[41] Adriano Ambrosi et al. "Enhancement of electrochemical and catalytic properties of MoS2 through ball-milling". In: *Electrochemistry Communications* 54 (2015), pp. 36–40. DOI: https://doi.org/10.1016/j.elecom.2015.02.017.

[42] Oleg D. Neikov. "Chapter 2 - Mechanical Crushing and Grinding". In: *Handbook of Non-Ferrous Metal Powders (Second Edition)* 2 (2019), pp. 65–90. DOI: https://doi.org/10.1016/B978-0-08-100543-9.00002-6.

[43] I. Wilkomirsky, J. Becker, and F. Parada. "Molybdenite Concentrate Purification by a Continuous Sulfation-Leaching Process". In: *Mining, Metallurgy & Exploration* 39 (2022), pp. 1679–1686. DOI: https://doi.org/10.1007/s42461-022-00628-7.

[44] Ikumapayi Fatai Kolawole. "Purification of molybdenite concentrates". MA thesis. 2008.

[45] Malvern Panalytical. "MASTERSIZER 3000 Smarter particle sizing". In: (), pp. 4–7. DOI: https://www.malvernpanalytical.com/en/assets/MRK1872-07-EN_MS3000_Broch_BrandUpdate_LR_web_tcm50-17232.pdf.

[46] Purdue University. *Scanning electron microscope*. URL: https://www.purdue.edu/ehps/rem/laboratory/equipment%5C%20safety/Research%5C%20Equipment/sem.html. (accessed: 08.05.2023).

[47] ThermoFischer Scientific. *Energy Dispersive Spectroscopy*. URL: https://www.thermofisher.com/no/en/home/materials-science/eds-technology.html. (accessed: 08.05.2023).

[48] Orion engineered carbons. *Batteries*. URL: https://orioncarbons.com/batteries. (accessed: 30.05.2023).

[49] nanografi.com. *PVDF binder for battery*. URL: https://nanografi.com/blog/pvdf-binder-for-battery/. (accessed: 30.05.2023).

[50] Xuehu Zhong et al. "Binding mechanisms of PVDF in lithium ion batteries". In: *Applied surface science* 553 (2021), pp. 1–5. DOI: https://doi.org/10.1016/j.apsusc.2021.149564.

[51] Colin Darcel. *What is NMP solvent?* URL: https://www.maratek.com/blog/what-is-nmp-solvent. (accessed: 30.05.2023).

[52] Andrew Kozbial et al. "Understanding the intrinsic water wettability of molybdenum disulfide (MoS_2)". In: *American chemical society* 31.30 (2015), pp. 8429–8435. DOI: https://doi.org/10.1021/acs.langmuir.5b02057.

Risk assesement

Task:	Preforming hot acid baked treatment on MoS2 sample
Created:	16.02.2023
Last updated:	23.02.2023
Last uppdated by:	Kristine Lehrmann Solvang
Task Description	Chemical purification of molybdenum disulfide with sulfuric acid below 160-190 degrees.

UNIVERSITY OF AGDER
FACULTY OF ENGINEERING AND SCIENCE

Identify hazardous events in all phases of the project			Given the exposure, what is negative outcome? (briefly describe)				Measures in the design phase to try to avoid "major changes"	Risk assessment according after **design measures**			Other necessary measures to reduce risk to an acceptable level	Risk assessment according to other measures			If the risk is medium 5-9, one must assess whether the measures taken are sufficient
Nr.	***Hazard***	***Hazardous situation***	**Consequence**	**S**	**P**	**Risk**	**Measures**	**S**	**P**	**Risk**	**Other measures**	**S**	**P**	**Risk**	**Assessment / Comment**
1	Handling sulfuric acid before baking, in crusibles	Spillage of sulfuric acid on skin, clothes, in eyes, or mouth	Severe burns on skin and eyes, can cause blindness. Can cause severe internal burns	4	3	**12**	Use gloves, mask and labratory coat when handling. Know that the substanse is dangerous and hanlde with care. Use safety goggles when filling. Keep information about what to do in an emergency available at all times.	3	2	**6**	Go trough safety yearly for all personel handling using the lab. Eye shower installed in the lab in case of emergency. If spilled wash with plenty of water and contact medical personell.	2	2	**4**	
2	Handling sulfuric acid before baking, in crusibles	Gasses forming when handling and acid being inhaled	Irritation in nose and lungs, fainting, dificulty breathing	4	3	**12**	Handle the acid in a well ventilated place, extractor hood or use mask. Knowing the emergency number.	3	2	**6**	Remove person to well ventilated area and contact medical personell. Keep safety information eaily available.	2	2	**4**	
3	Heating and cooling samlpes on hotplate to 180C	Burning skin on the hotplate or equipment on/around hotplate, gases from sulfuric acid developing in extraction hood	Severe burns to skin, inhaling gas	4	3	**12**	Being aware of the temperature of the oven and acting responsible around it when hot. When handling equipment near/in oven use gloves. Be careful when opening oven, use oven in well ventilated area. Let procedure go at night. Don't let any unothorized personel in room when treatement is started. Let the samples cool of before opening the oven.	2	2	**4**	Keep safety information available at lab. Contact medical personell if spillage on skin and in eyes. Have emergency shower installed. If spilled wash with plenty of water.	2	1	**2**	
4	Handling beaker after treatment	Spilling sulfuric acid, handling the full beaker, breaker breaking on hotplate or when handeled	Spilling on skin causing severe burns, blindness, oven contaminated	4	3	**12**	Carefuly handling the beaker, using gloves. Make sure the temperature on the hotplate and of samples is low by measuring with a laser.	3	3	**9**	If burned wash with water, keep emergency shower and eye shower close by and check if functional regularly. Regularly check if hotplate is working correctly.	3	2	**6**	
5	Handling sulfuric acid after treatment, when washing	Spillage of sulfuric acid on skin, clothes, in eyes, or mouth	Severe burns on skin and eyes, can cause blindness. Can cause severe internal burns	4	3	**12**	Use gloves when handling, minimize distance of carying the samples. Handle in extractor hood.	2	3	**6**	if any spillage on skin wash with plenty of water and contact medical personell	2	2	**4**	
6	Getting rid of acid when done	Corrosive reactions on drain, fumes from chemicals when handeled	Damage on drains, inhaling, fire	3	3	**9**	The acid is to be handeled with care, Disvolve in water and keep in closed container. Handeled as special waste.	2	3	**6**	Keep waste bins marked properly and close by so transportation distance is minimized.	2	2	**4**	
7						**0**				**0**				**0**	
8						**0**				**0**				**0**	
9						**0**				**0**				**0**	
10						**0**				**0**				**0**	
11						**0**				**0**				**0**	
12						**0**				**0**					
13															
14															

Responsible project manager:

Responsible lab manager:

A copy of the signed analysis must be submitted to the HSE representative

Analysis

Malvern Instruments

Malvern

Measurement Details	
Operator Name	Lab
Sample Name	MoS2_knaben_milled_24h_batch3
SOP File Name	HydroEV.cfg

Measurement Details	
Analysis Date Time	3/15/2023 1:18:14 PM
Measurement Date Time	3/15/2023 1:18:14 PM
Result Source	Measurement

Analysis	
Particle Name	Molybdenium disulfide (MoS2)
Particle Refractive Index	4.500
Particle Absorption Index	1.000
Dispersant Name	Water
Dispersant Refractive Index	1.330
Scattering Model	Mie
Analysis Model	General Purpose
Weighted Residual	3.66 %
Laser Obscuration	5.34 %

Result	
Concentration	0.0036 %
Span	18.364
Uniformity	4.343
Specific Surface Area	201.7 m²/kg
D [3,2]	5.88 µm
D [4,3]	129 µm
Dv (10)	2.34 µm
Dv (50)	27.4 µm
Dv (90)	506 µm

Frequency (compatible)

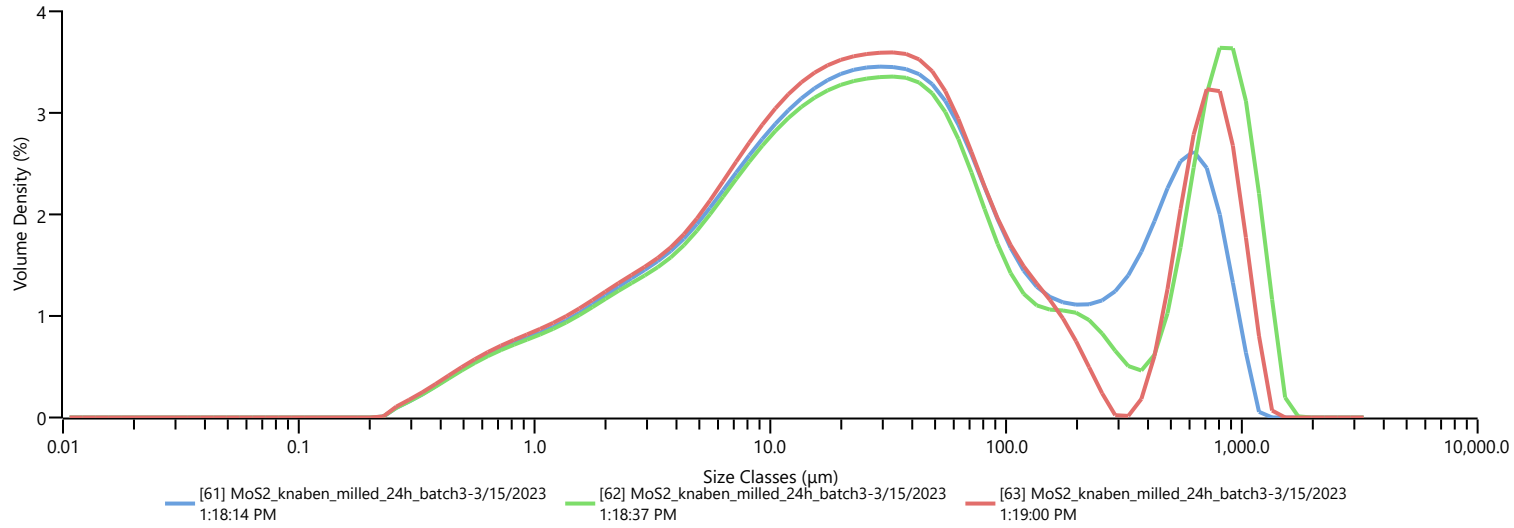

Result

Size (µm)	% Volume In	Size (µm)	% Volume In	Size (µm)	% Volume In	Size (µm)	% Volume In	Size (µm)	% Volume In	Size (µm)	% Volume In	Size (µm)	% Volume In	Size (µm)	% Volume In
0.0100	0.00	0.0597	0.00	0.357	0.26	2.13	1.07	12.7	2.62	76.0	1.89	454	1.89	2710	0.00
0.0114	0.00	0.0679	0.00	0.405	0.33	2.42	1.14	14.5	2.70	86.4	1.63	516	2.12	3080	0.00
0.0129	0.00	0.0771	0.00	0.460	0.39	2.75	1.21	16.4	2.77	98.1	1.39	586	2.20	3500	
0.0147	0.00	0.0876	0.00	0.523	0.46	3.12	1.28	18.7	2.82	111	1.20	666	2.07		
0.0167	0.00	0.0995	0.00	0.594	0.52	3.55	1.37	21.2	2.86	127	1.07	756	1.68		
0.0189	0.00	0.113	0.00	0.675	0.57	4.03	1.47	24.1	2.87	144	0.99	859	1.11		
0.0215	0.00	0.128	0.00	0.767	0.61	4.58	1.59	27.4	2.88	163	0.94	976	0.53		
0.0244	0.00	0.146	0.00	0.872	0.65	5.21	1.72	31.1	2.88	186	0.92	1110	0.00		
0.0278	0.00	0.166	0.00	0.991	0.70	5.92	1.87	35.3	2.86	211	0.93	1260	0.00		
0.0315	0.00	0.188	0.00	1.13	0.74	6.72	2.01	40.1	2.82	240	0.96	1430	0.00		
0.0358	0.00	0.214	0.00	1.28	0.80	7.64	2.15	45.6	2.74	272	1.03	1630	0.00		
0.0407	0.00	0.243	0.08	1.45	0.86	8.68	2.29	51.8	2.60	310	1.16	1850	0.00		
0.0463	0.00	0.276	0.13	1.65	0.93	9.86	2.41	58.9	2.41	352	1.36	2100	0.00		
0.0526	0.00	0.314	0.19	1.88	1.00	11.2	2.52	66.9	2.16	400	1.61	2390	0.00		

Analysis

Malvern Instruments

Measurement Details	
Operator Name	Lab
Sample Name	Average of 'MoS2_knaben_ballmill48h_ny'
SOP File Name	HydroEV.cfg

Measurement Details	
Analysis Date Time	3/6/2023 10:47:26 AM
Measurement Date Time	3/6/2023 10:47:26 AM
Result Source	Averaged

Analysis	
Particle Name	[BROWSE]
Particle Refractive Index	4.500
Particle Absorption Index	1.000
Dispersant Name	Water
Dispersant Refractive Index	1.330
Scattering Model	Mie
Analysis Model	General Purpose
Weighted Residual	1.05 %
Laser Obscuration	14.60 %

Result	
Concentration	0.0103 %
Span	8.316
Uniformity	2.904
Specific Surface Area	201.9 m²/kg
D [3,2]	5.87 µm
D [4,3]	89.6 µm
Dv (10)	2.29 µm
Dv (50)	27.5 µm
Dv (90)	231 µm

Frequency (compatible)

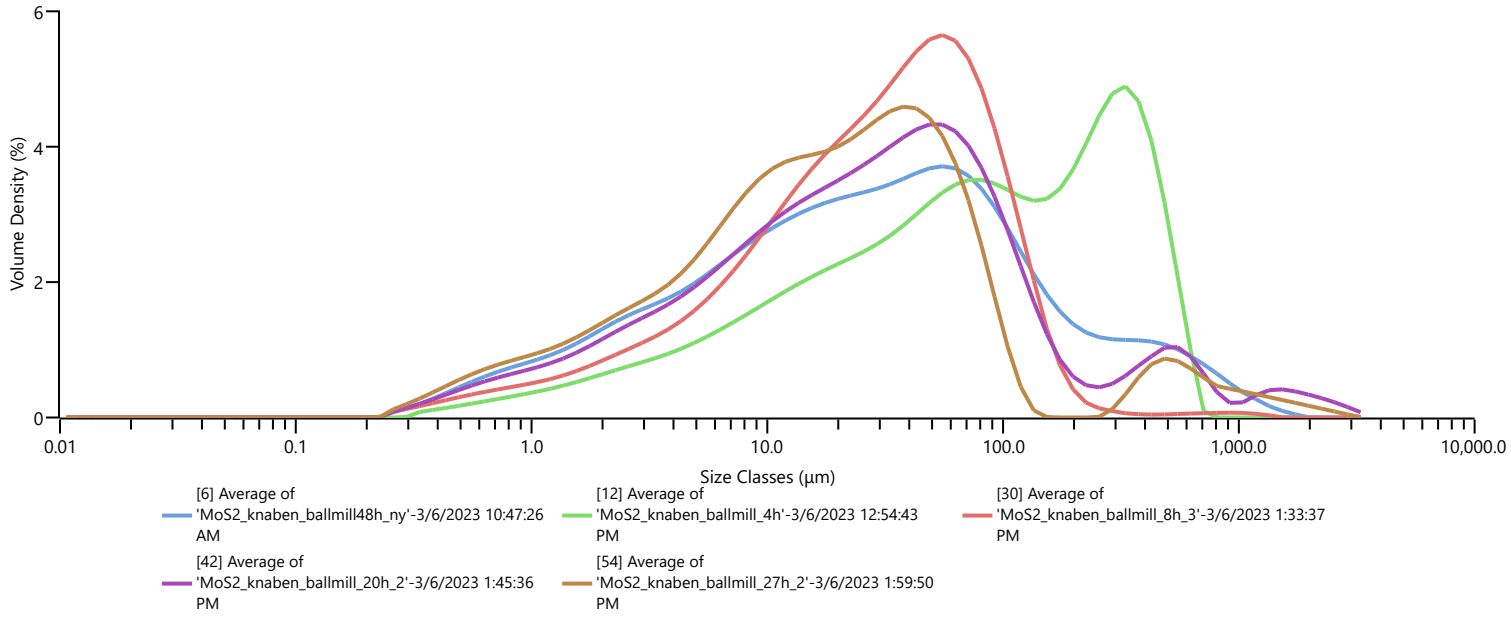

Result

Size (µm)	% Volume In	Size (µm)	% Volume In	Size (µm)	% Volume In	Size (µm)	% Volume In	Size (µm)	% Volume In	Size (µm)	% Volume In	Size (µm)	% Volume In	Size (µm)	% Volume In
0.0100	0.00	0.0597	0.00	0.357	0.23	2.13	1.18	12.7	2.51	76.0	2.82	454	0.90	2710	0.00
0.0114	0.00	0.0679	0.00	0.405	0.30	2.42	1.26	14.5	2.58	86.4	2.60	516	0.84	3080	0.00
0.0129	0.00	0.0771	0.00	0.460	0.37	2.75	1.33	16.4	2.64	98.1	2.33	586	0.76	3500	
0.0147	0.00	0.0876	0.00	0.523	0.44	3.12	1.40	18.7	2.69	111	2.04	666	0.65		
0.0167	0.00	0.0995	0.00	0.594	0.51	3.55	1.47	21.2	2.73	127	1.76	756	0.54		
0.0189	0.00	0.113	0.00	0.675	0.56	4.03	1.55	24.1	2.77	144	1.51	859	0.42		
0.0215	0.00	0.128	0.00	0.767	0.62	4.58	1.65	27.4	2.82	163	1.30	976	0.31		
0.0244	0.00	0.146	0.00	0.872	0.66	5.21	1.76	31.1	2.87	186	1.15	1110	0.22		
0.0278	0.00	0.166	0.00	0.991	0.71	5.92	1.88	35.3	2.94	211	1.04	1260	0.14		
0.0315	0.00	0.188	0.00	1.13	0.77	6.72	2.01	40.1	3.01	240	0.99	1430	0.08		
0.0358	0.00	0.214	0.00	1.28	0.83	7.64	2.12	45.6	3.07	272	0.96	1630	0.04		
0.0407	0.00	0.243	0.07	1.45	0.91	8.68	2.23	51.8	3.10	310	0.96	1850	0.00		
0.0463	0.00	0.276	0.11	1.65	1.00	9.86	2.33	58.9	3.07	352	0.95	2100	0.00		
0.0526	0.00	0.314	0.17	1.88	1.09	11.2	2.43	66.9	2.98	400	0.94	2390	0.00		

Analysis

Malvern Instruments

Malvern

Measurement Details	
Operator Name	Lab
Sample Name	Average of 'MoS2_knaben_ballmill48h_ny'
SOP File Name	HydroEV.cfg

Measurement Details	
Analysis Date Time	3/6/2023 10:47:26 AM
Measurement Date Time	3/6/2023 10:47:26 AM
Result Source	Averaged

Analysis	
Particle Name	[BROWSE]
Particle Refractive Index	4.500
Particle Absorption Index	1.000
Dispersant Name	Water
Dispersant Refractive Index	1.330
Scattering Model	Mie
Analysis Model	General Purpose
Weighted Residual	1.05 %
Laser Obscuration	14.60 %

Result	
Concentration	0.0103 %
Span	8.316
Uniformity	2.904
Specific Surface Area	201.9 m²/kg
D [3,2]	5.87 µm
D [4,3]	89.6 µm
Dv (10)	2.29 µm
Dv (50)	27.5 µm
Dv (90)	231 µm

Frequency (compatible)

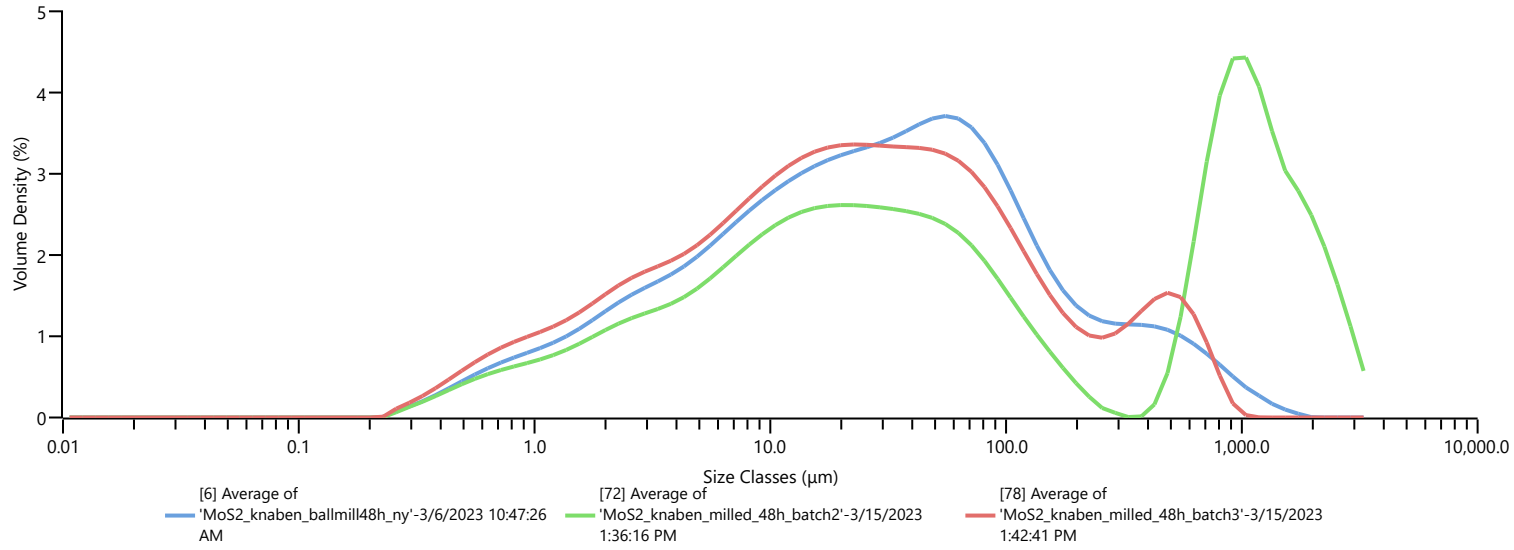

Result

Size (µm)	% Volume In	Size (µm)	% Volume In	Size (µm)	% Volume In	Size (µm)	% Volume In	Size (µm)	% Volume In	Size (µm)	% Volume In	Size (µm)	% Volume In	Size (µm)	% Volume In
0.0100	0.00	0.0597	0.00	0.357	0.23	2.13	1.18	12.7	2.51	76.0	2.82	454	0.90	2710	0.00
0.0114	0.00	0.0679	0.00	0.405	0.30	2.42	1.26	14.5	2.58	86.4	2.60	516	0.84	3080	0.00
0.0129	0.00	0.0771	0.00	0.460	0.37	2.75	1.33	16.4	2.64	98.1	2.33	586	0.76	3500	
0.0147	0.00	0.0876	0.00	0.523	0.44	3.12	1.40	18.7	2.69	111	2.04	666	0.65		
0.0167	0.00	0.0995	0.00	0.594	0.51	3.55	1.47	21.2	2.73	127	1.76	756	0.54		
0.0189	0.00	0.113	0.00	0.675	0.56	4.03	1.55	24.1	2.77	144	1.51	859	0.42		
0.0215	0.00	0.128	0.00	0.767	0.62	4.58	1.65	27.4	2.82	163	1.30	976	0.31		
0.0244	0.00	0.146	0.00	0.872	0.66	5.21	1.76	31.1	2.87	186	1.15	1110	0.22		
0.0278	0.00	0.166	0.00	0.991	0.71	5.92	1.88	35.3	2.94	211	1.04	1260	0.14		
0.0315	0.00	0.188	0.00	1.13	0.77	6.72	2.01	40.1	3.01	240	0.99	1430	0.08		
0.0358	0.00	0.214	0.00	1.28	0.83	7.64	2.12	45.6	3.07	272	0.96	1630	0.04		
0.0407	0.00	0.243	0.07	1.45	0.91	8.68	2.23	51.8	3.10	310	0.96	1850	0.00		
0.0463	0.00	0.276	0.11	1.65	1.00	9.86	2.33	58.9	3.07	352	0.95	2100	0.00		
0.0526	0.00	0.314	0.17	1.88	1.09	11.2	2.43	66.9	2.98	400	0.94	2390	0.00		

Analysis

Malvern Instruments

Measurement Details	
Operator Name	Lab
Sample Name	MoS2_knaben_milled_24h_pure_3
SOP File Name	HydroEV.cfg

Measurement Details	
Analysis Date Time	3/15/2023 1:58:14 PM
Measurement Date Time	3/15/2023 1:58:14 PM
Result Source	Measurement

Analysis	
Particle Name	Molybdenium disulfide (MoS2)
Particle Refractive Index	4.500
Particle Absorption Index	1.000
Dispersant Name	Water
Dispersant Refractive Index	1.330
Scattering Model	Mie
Analysis Model	General Purpose
Weighted Residual	3.86 %
Laser Obscuration	7.29 %

Result	
Concentration	0.0064 %
Span	3.308
Uniformity	1.019
Specific Surface Area	291.2 m²/kg
D [3,2]	4.07 µm
D [4,3]	18.6 µm
Dv (10)	1.52 µm
Dv (50)	13.1 µm
Dv (90)	44.7 µm

Frequency (compatible)

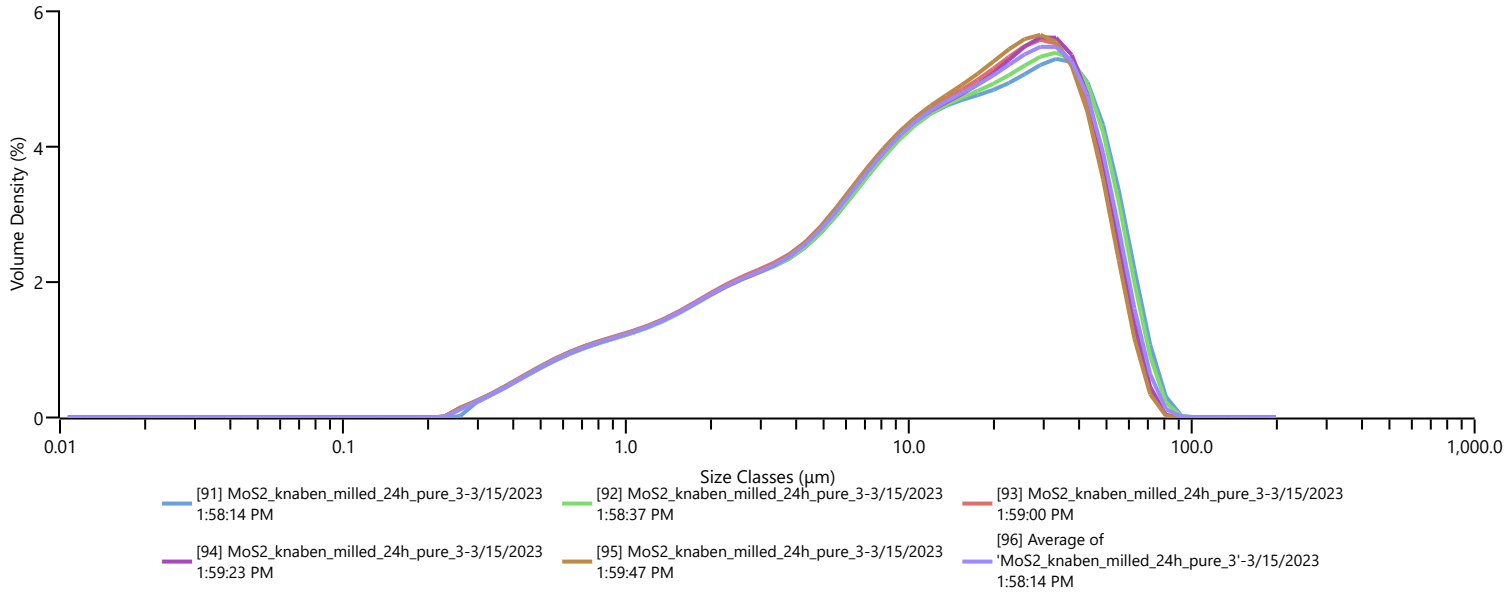

Result

Size (µm)	% Volume In	Size (µm)	% Volume In	Size (µm)	% Volume In	Size (µm)	% Volume In	Size (µm)	% Volume In	Size (µm)	% Volume In	Size (µm)	% Volume In	Size (µm)	% Volume In
0.0100	0.00	0.0597	0.00	0.357	0.38	2.13	1.62	12.7	3.84	76.0	0.22	454	0.00	2710	0.00
0.0114	0.00	0.0679	0.00	0.405	0.49	2.42	1.71	14.5	3.91	86.4	0.00	516	0.00	3080	0.00
0.0129	0.00	0.0771	0.00	0.460	0.59	2.75	1.78	16.4	3.97	98.1	0.00	586	0.00	3500	
0.0147	0.00	0.0876	0.00	0.523	0.70	3.12	1.86	18.7	4.03	111	0.00	666	0.00		
0.0167	0.00	0.0995	0.00	0.594	0.78	3.55	1.95	21.2	4.12	127	0.00	756	0.00		
0.0189	0.00	0.113	0.00	0.675	0.86	4.03	2.09	24.1	4.23	144	0.00	859	0.00		
0.0215	0.00	0.128	0.00	0.767	0.92	4.58	2.27	27.4	4.34	163	0.00	976	0.00		
0.0244	0.00	0.146	0.00	0.872	0.98	5.21	2.49	31.1	4.43	186	0.00	1110	0.00		
0.0278	0.00	0.166	0.00	0.991	1.04	5.92	2.73	35.3	4.40	211	0.00	1260	0.00		
0.0315	0.00	0.188	0.00	1.13	1.11	6.72	2.98	40.1	4.16	240	0.00	1430	0.00		
0.0358	0.00	0.214	0.00	1.28	1.20	7.64	3.21	45.6	3.63	272	0.00	1630	0.00		
0.0407	0.00	0.243	0.00	1.45	1.30	8.68	3.43	51.8	2.81	310	0.00	1850	0.00		
0.0463	0.00	0.276	0.19	1.65	1.41	9.86	3.61	58.9	1.82	352	0.00	2100	0.00		
0.0526	0.00	0.314	0.28	1.88	1.52	11.2	3.74	66.9	0.87	400	0.00	2390	0.00		

Marlene

Author: Cecilie
Creation: 03/20/2023 3:05:54 PM

Sample Name: MoS2-C_pure2023-Kristine

Area 3

Live Map 1

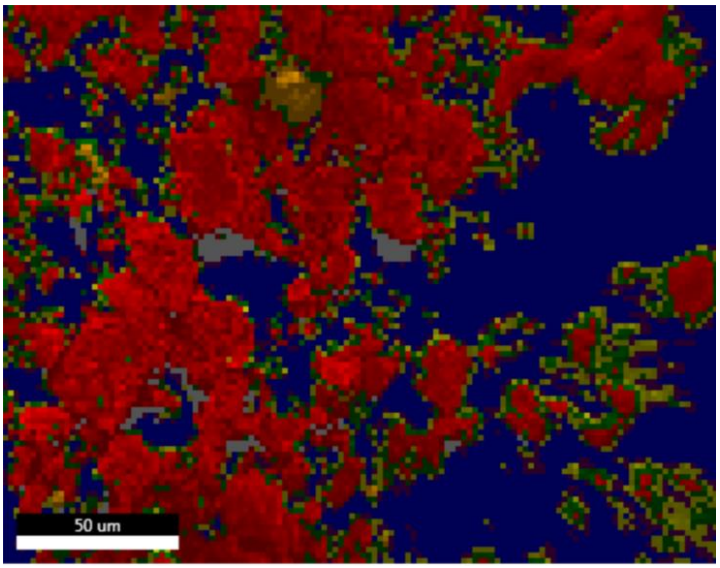

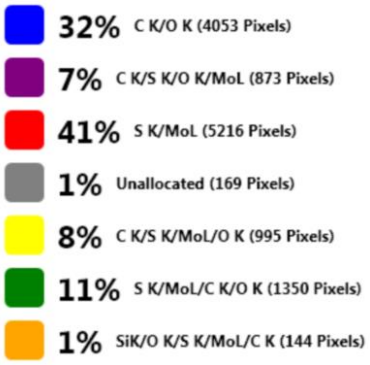

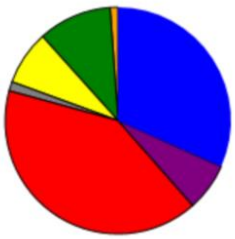

Notes:

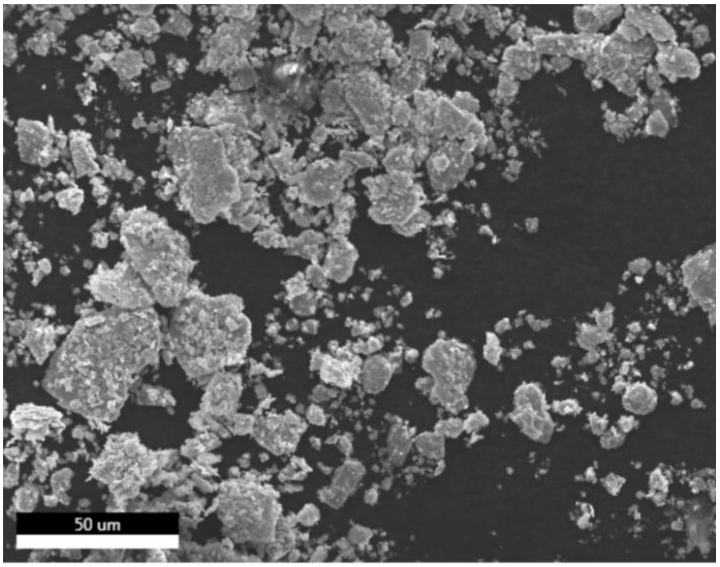

Image

ElementOverlay

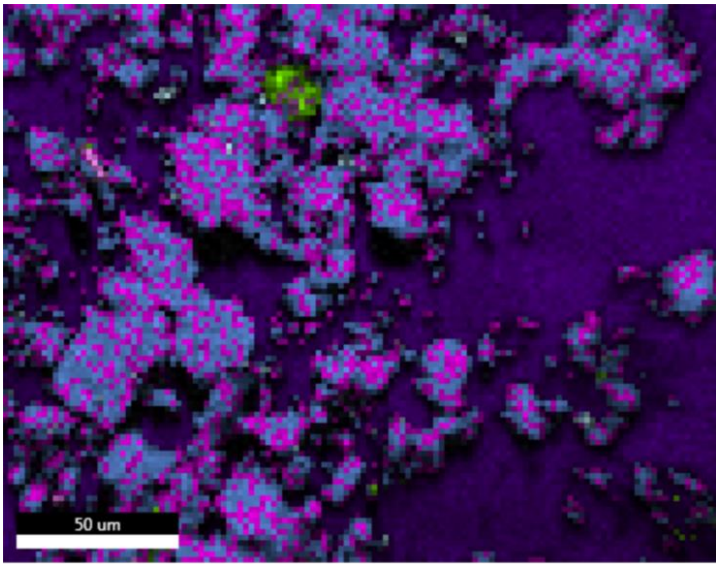

37% C K
7% O K
2% AlK
3% SiK
23% MoL
29% S K

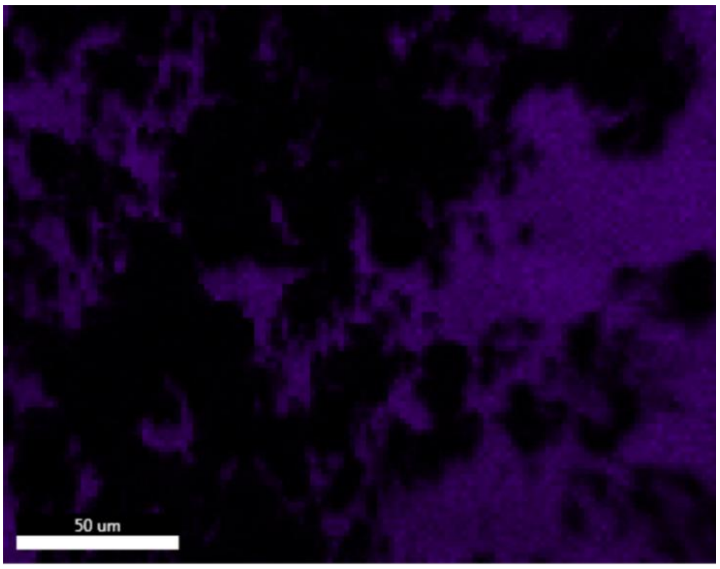

C K_ROI (202)

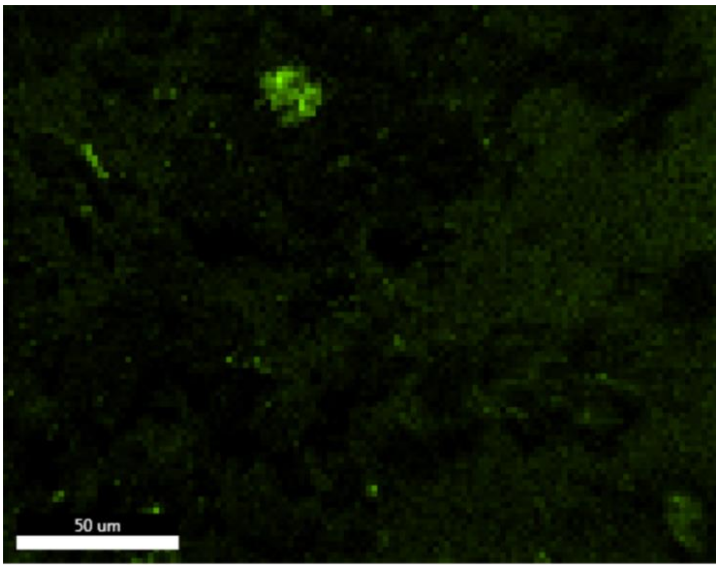

O K_ROI (168)

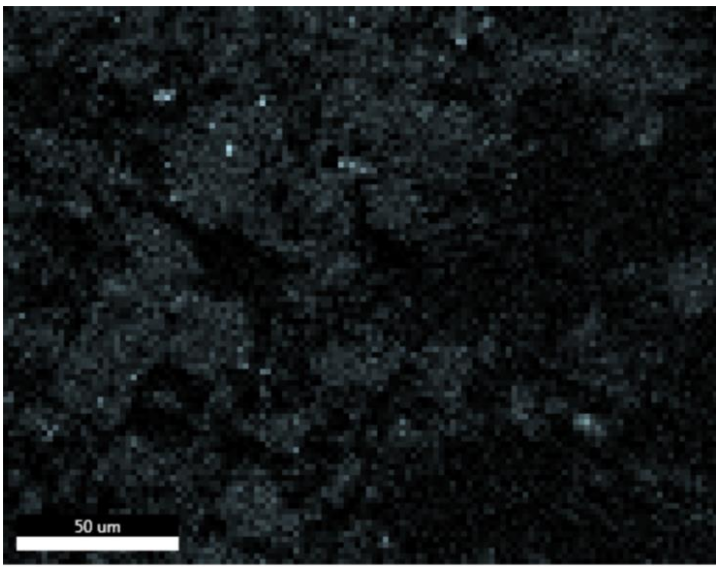

AlK_ROI (43)

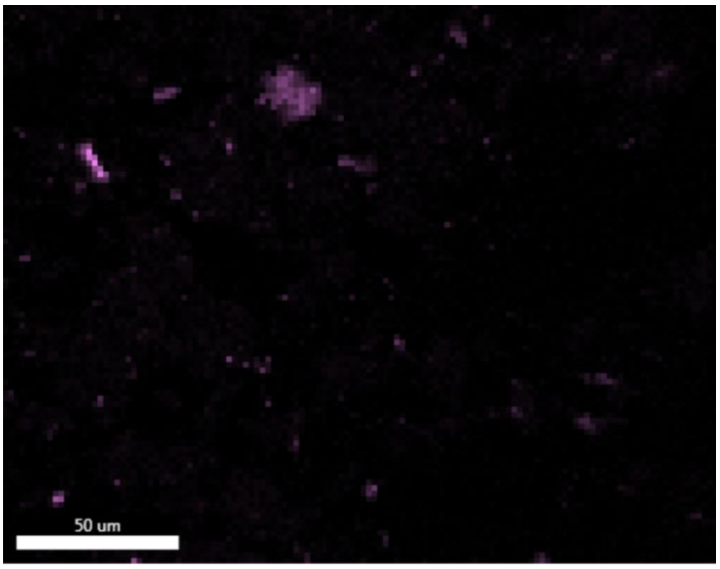

SiK_ROI (226)

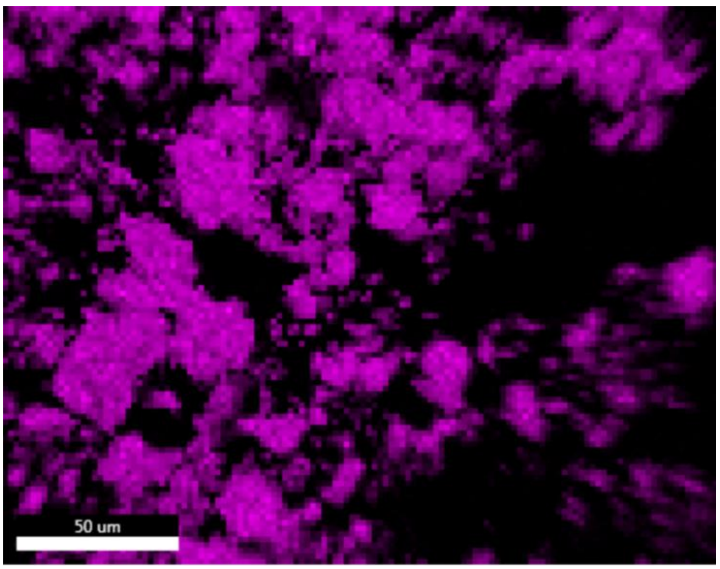

MoL_ROI (212)

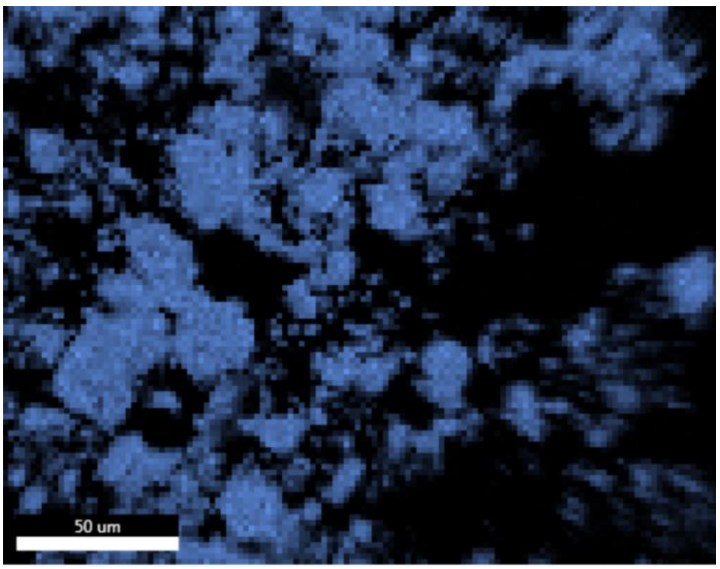

S K_ROI (261)

kV:	15	Mag:500	Takeoff: 30	Live Time(s): 440.3	Amp Time(µs): 1.92	Resolution:(eV) 125.6

Sum Spectrum

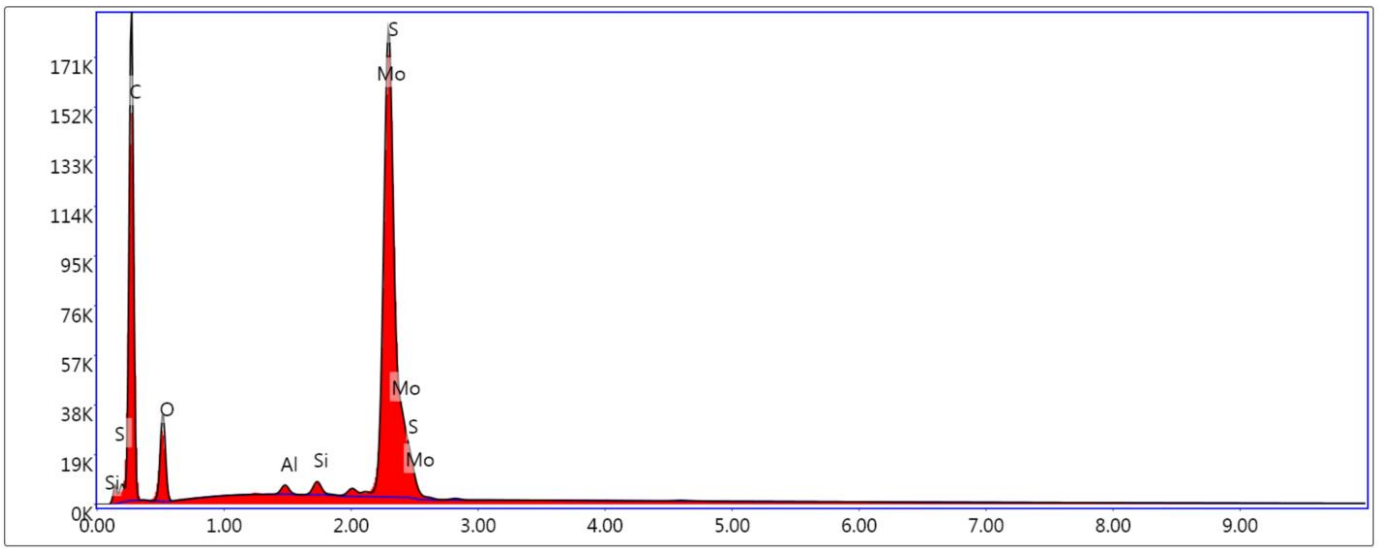

Lsec: 440.3 137.748K Cnts 0.270 keV Det: Octane Elect Plus

eZAF Smart Quant Results

Element	Weight %	Atomic %	Net Int.	Error %	Kratio	Z	A	F
C K	61.8	81.1	1798.5	9.0	0.1540	1.0775	0.2311	1.0000
O K	10.0	9.9	365.5	10.2	0.0148	1.0272	0.1436	1.0000
AlK	0.3	0.2	59.4	4.6	0.0021	0.9080	0.8136	1.0068
SiK	0.4	0.2	92.7	3.7	0.0033	0.9270	0.8949	1.0109
MoL	14.7	2.4	1342.1	3.0	0.1160	0.6926	1.1408	0.9994
S K	12.8	6.3	2339.2	1.8	0.1145	0.9063	0.9800	1.0083

kV:	15	Mag:500	Takeoff: 30	Live Time(s): 139.4	Amp Time(µs): 1.92	Resolution:(eV) 125.6

Phase: **C K/O K**

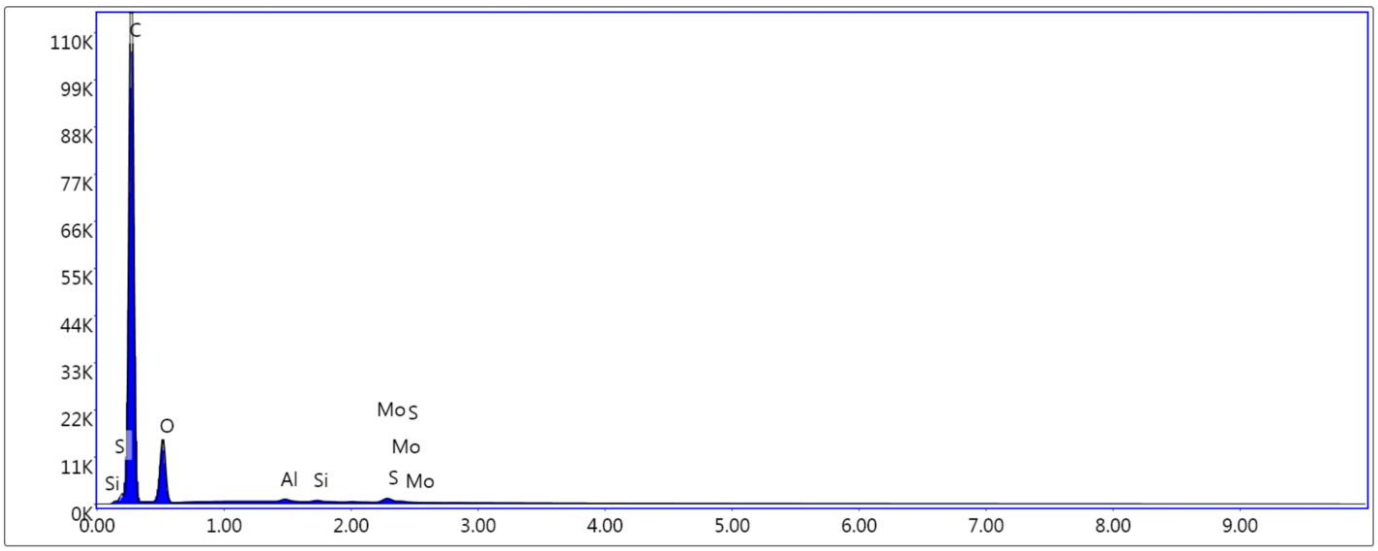

Lsec: 139.4 97.130K Cnts 0.270 keV Det: Octane Elect Plus

eZAF Smart Quant Results

Element	Weight %	Atomic %	Net Int.	Error %	Kratio	Z	A	F
C K	76.9	82.3	4114.2	3.8	0.5853	1.0148	0.7500	1.0000
O K	21.6	17.3	519.4	10.4	0.0349	0.9644	0.1677	1.0000
AlK	0.3	0.1	31.7	6.5	0.0018	0.8484	0.8377	1.0042
SiK	0.1	0.1	18.9	8.6	0.0011	0.8656	0.9178	1.0066
MoL	1.2	0.2	61.1	8.5	0.0088	0.6458	1.1680	0.9997
S K	0.0	0.0	0.0	100.0	0.0000	0.8451	0.9981	1.0148

kV:	15	Mag:500	Takeoff: 30	Live Time(s): 30	Amp Time(µs): 1.92	Resolution:(eV) 125.6

Phase: **C K/S K/O K/MoL**

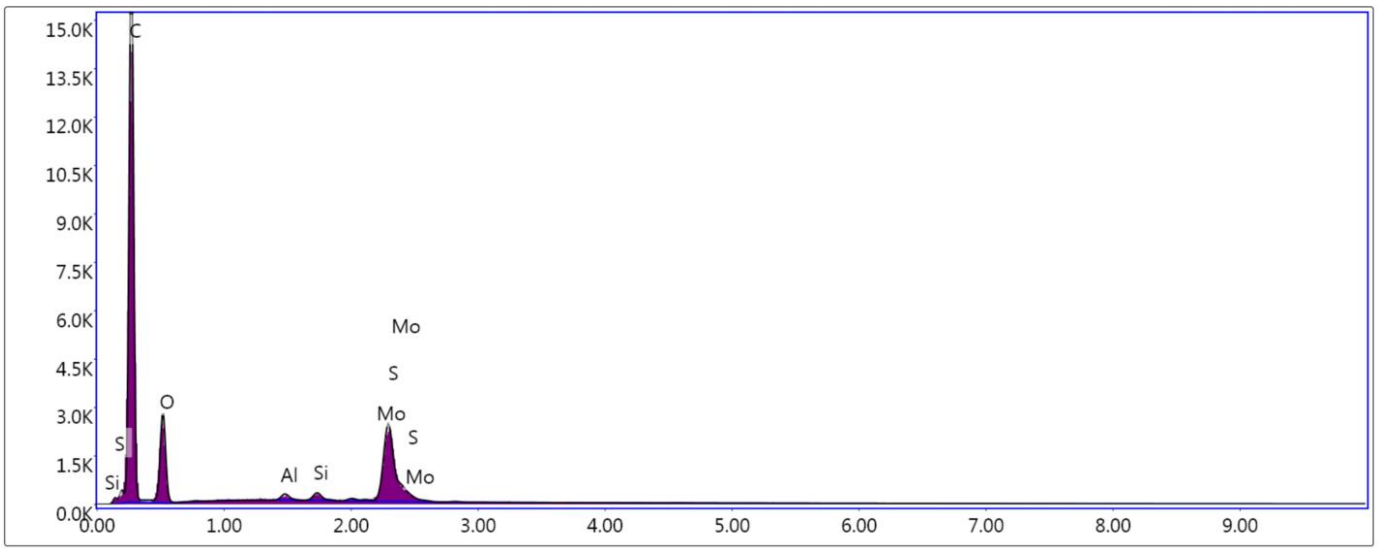

Lsec: 30.0 12.494K Cnts 0.270 keV Det: Octane Elect Plus

eZAF Smart Quant Results

Element	Weight %	Atomic %	Net Int.	Error %	Kratio	Z	A	F
C K	71.6	81.8	2523.7	7.0	0.3379	1.0356	0.4559	1.0000
O K	18.0	15.4	444.5	11.5	0.0281	0.9853	0.1585	1.0000
AlK	0.3	0.2	43.2	11.4	0.0023	0.8684	0.8261	1.0057
SiK	0.4	0.2	59.7	9.9	0.0034	0.8862	0.9068	1.0090
MoL	6.2	0.9	350.4	4.9	0.0474	0.6616	1.1555	0.9996
S K	3.5	1.5	397.3	3.2	0.0304	0.8657	0.9890	1.0116

kV:	15	Mag:500	Takeoff: 30	Live Time(s): 179.4	Amp Time(µs): 1.92	Resolution:(eV) 125.6

Phase: **S K/MoL**

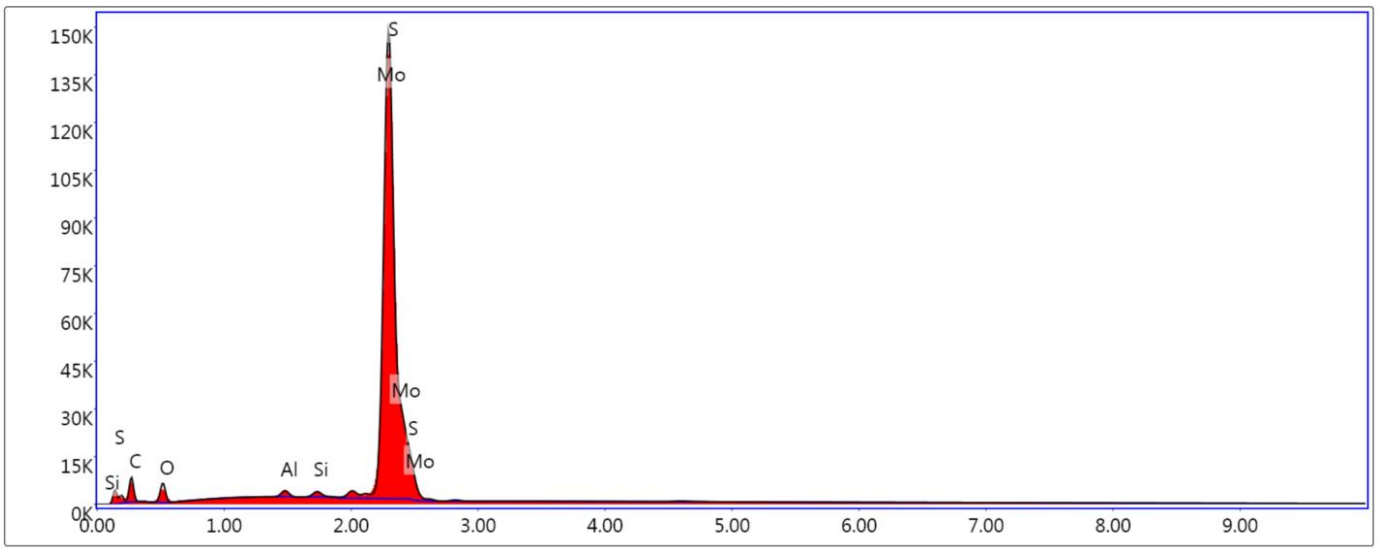

Lsec: 179.4 6.596K Cnts 0.270 keV Det: Octane Elect Plus

eZAF Smart Quant Results

Element	Weight %	Atomic %	Net Int.	Error %	Kratio	Z	A	F
C K	18.0	44.1	171.0	11.0	0.0221	1.2398	0.0989	1.0000
O K	5.9	10.8	154.6	11.1	0.0094	1.1863	0.1346	1.0000
AlK	0.5	0.5	72.4	6.4	0.0038	1.0554	0.7412	1.0073
SiK	0.4	0.4	68.7	6.2	0.0037	1.0787	0.8305	1.0119
MoL	40.6	12.4	2718.1	2.4	0.3548	0.8078	1.0837	0.9992
S K	34.6	31.7	4670.6	2.2	0.3454	1.0566	0.9380	1.0067

kV:	15	Mag:500	Takeoff: 30	Live Time(s): 5.8	Amp Time(µs): 1.92	Resolution:(eV) 125.6

Phase: **Unallocated**

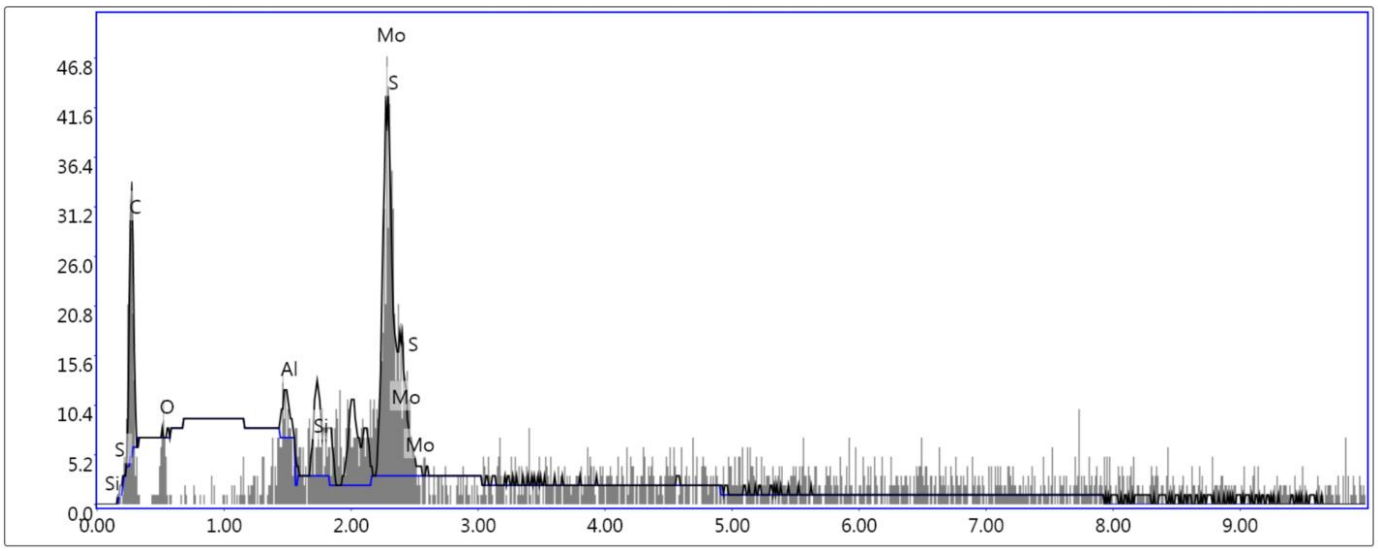

Lsec: 5.8 32 Cnts 0.270 keV Det: Octane Elect Plus

eZAF Smart Quant Results

Element	Weight %	Atomic %	Net Int.	Error %	Kratio	Z	A	F
C K	46.0	75.6	28.2	20.8	0.1375	1.1611	0.2573	1.0000
O K	10.7	13.2	7.0	49.0	0.0162	1.1100	0.1366	1.0000
AlK	2.8	2.0	10.4	50.8	0.0204	0.9860	0.7449	1.0058
SiK	1.8	1.2	7.1	67.8	0.0146	1.0075	0.8175	1.0088
MoL	38.8	8.0	64.0	16.7	0.3154	0.7540	1.0789	0.9999
S K	0.1	0.0	0.2	100.0	0.0005	0.9864	0.9245	1.0177

kV:	15	Mag:500	Takeoff: 30	Live Time(s): 34.2	Amp Time(µs): 1.92	Resolution:(eV) 125.6

Phase: **C K/S K/MoL/O K**

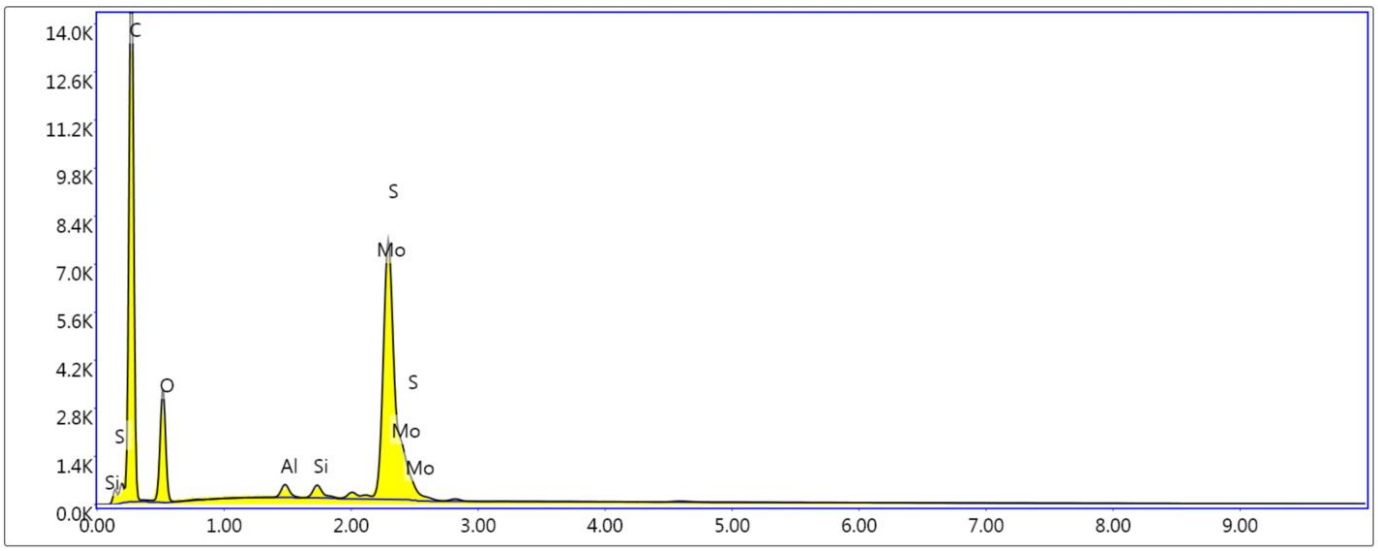

Lsec: 34.2 12.156K Cnts 0.270 keV Det: Octane Elect Plus

eZAF Smart Quant Results

Element	Weight %	Atomic %	Net Int.	Error %	Kratio	Z	A	F
C K	64.9	80.6	2100.2	8.5	0.2133	1.0617	0.3094	1.0000
O K	14.6	13.6	465.7	11.1	0.0223	1.0115	0.1508	1.0000
AlK	0.4	0.2	69.2	8.6	0.0028	0.8932	0.8121	1.0062
SiK	0.4	0.2	77.5	7.4	0.0033	0.9118	0.8938	1.0100
MoL	12.2	1.9	929.0	3.7	0.0953	0.6811	1.1435	0.9996
S K	7.4	3.5	1126.7	2.4	0.0655	0.8912	0.9804	1.0102

kV:	15	Mag:500	Takeoff: 30	Live Time(s): 46.4	Amp Time(µs): 1.92	Resolution:(eV) 125.6

Phase: **S K/MoL/C K/O K**

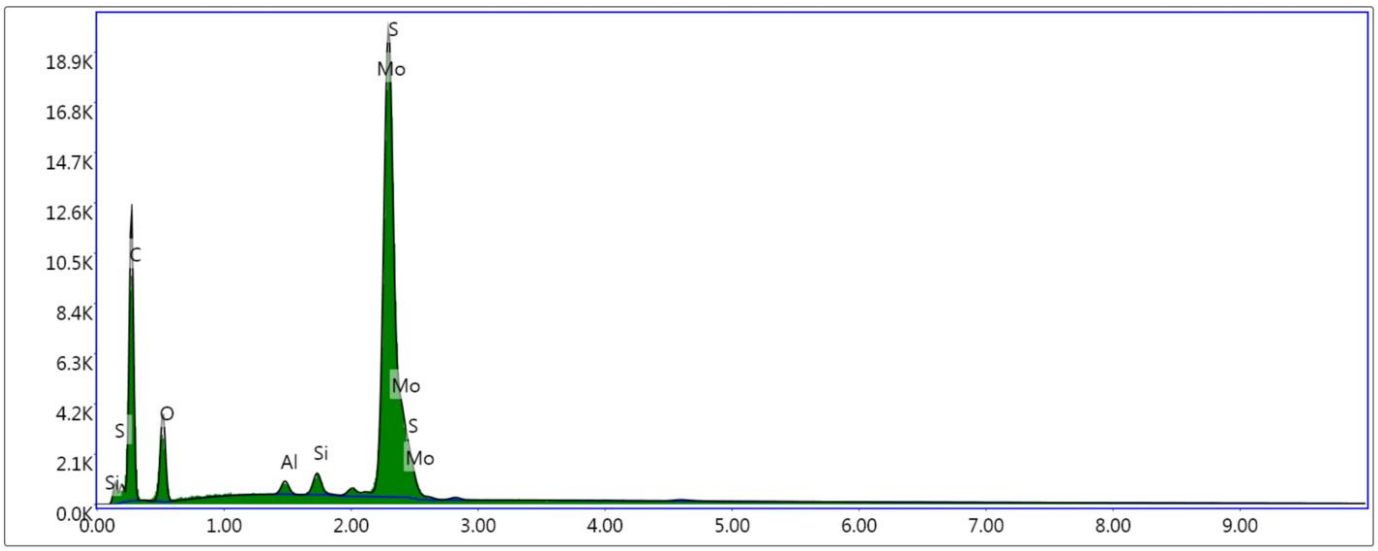

Lsec: 46.4 8.938K Cnts 0.270 keV Det: Octane Elect Plus

eZAF Smart Quant Results

Element	Weight %	Atomic %	Net Int.	Error %	Kratio	Z	A	F
C K	51.8	74.6	1089.7	9.7	0.1115	1.1047	0.1948	1.0000
O K	12.1	13.1	387.4	10.9	0.0187	1.0541	0.1464	1.0000
AlK	0.5	0.3	88.3	7.2	0.0037	0.9332	0.7915	1.0067
SiK	0.8	0.5	155.1	5.4	0.0067	0.9530	0.8748	1.0106
MoL	20.1	3.6	1555.8	3.2	0.1607	0.7124	1.1229	0.9994
S K	14.7	7.9	2275.6	2.2	0.1332	0.9321	0.9655	1.0083

kV:	15	Mag:500	Takeoff: 30	Live Time(s): 5	Amp Time(µs): 1.92	Resolution:(eV) 125.6

Phase: SiK/O K/S K/MoL/C K

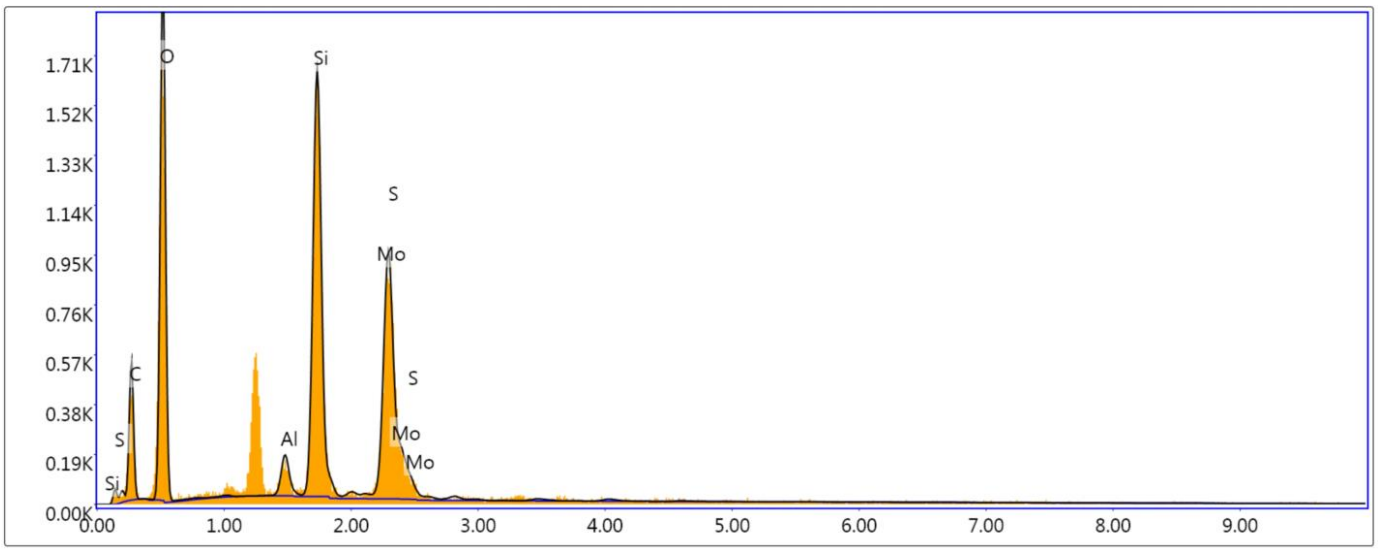

Lsec: 5.0 400 Cnts 0.270 keV Det: Octane Elect Plus

eZAF Smart Quant Results

Element	Weight %	Atomic %	Net Int.	Error %	Kratio	Z	A	F
C K	24.5	36.9	449.5	12.1	0.0479	1.0981	0.1785	1.0000
O K	40.9	46.3	2074.3	10.0	0.1044	1.0468	0.2442	1.0000
AlK	1.4	0.9	228.5	9.6	0.0099	0.9252	0.7648	1.0070
SiK	14.6	9.4	2623.9	3.9	0.1179	0.9445	0.8488	1.0055
MoL	11.0	2.1	734.9	6.1	0.0791	0.7056	1.0205	0.9991
S K	7.7	4.3	1022.1	5.0	0.0623	0.9232	0.8742	1.0060